Fundamentals and Technology of Surface-enhanced Raman Spectroscopy Through the Fabrication and Manipulation of Plasmonic Gold Metal Nanoparticle Dimers

by
Kristen Delane Alexander

A dissertation submitted to the faculty of the University of North Carolina at Chapel Hill in partial fulfillment of the requirements for the degree of Doctor of Philosophy in the Department of Physics and Astronomy.

Chapel Hill
2011

Approved by:

Dr. Rene Lopez, Advisor

Dr. Laurie McNeil, Reader

Dr. Royce Murray, Reader

Dr. Richard Superfine, Reader

Dr. Charles Evans, Reader

ABSTRACT
KRISTEN DELANE ALEXANDER: Fundamentals and Technology of Surface-enhanced Raman Spectroscopy Through the Fabrication and Manipulation of Plasmonic Gold Metal Nanoparticle Dimers. (Under the direction of Dr. Rene Lopez.)

Surface enhanced Raman spectroscopy (SERS) was originally discovered in the 1970s with the observation that organic molecules adsorbed onto a metal surface exhibit greatly enhanced Raman scattered light intensities when illuminated with a laser source. Enhancements of $\approx 10^6$ over regular Raman scattering have been commonly observed and proposed applications of SERS-active sensors exist over a wide range of fields, including chemical analysis, healthcare, food safety and national security, spurring an intense scientific interest in the area. More recently, observations of single-molecule SERS have demonstrated enhancement factors greater than 10^{13} at random 'hot spots', but so far, these enhancement factors are poorly understood due to lack of reproducibility and lack of methodical characterization of such spots. Theoretical calculations have shown that the dominant field enhancements are specifically localized in the crevices between metal nanoparticles and are strongly dependent on particle morphology, excitation wavelength and, perhaps above all, particle-particle coupling. The focus of this thesis is to address experimentally theoretical predictions by fabricating SERS configurations and to make definitive measurements of the SERS magnitude at interparticle hot spots. In this work, metal nanoparticles have been directed to form ordered arrays exclusively of metal nanoparticle dimers with control over orientation, size and interparticle spacing. In order to achieve unprecedented control of the material and geometric variables, elastomeric

substrates were used to change particle-particle distance while holding all other physical parameters constant. This fundamental new approach to hot spot creation has opened doors to a new family of SERS substrates, where the turning on/off of a hot spot is as easy as flipping a switch. Most recently, I have demonstrated the feasibility of this approach with long nanorods that show an outstanding theoretical SERS match with the characteristic polarization dependence expected of such nanostructures. Additionally, this thesis demonstrates the feasibility of creating SERS-active dimers over a large area using a capillary force deposition technique which has further been used to compare the SERS enhancement factors derived from dimers to those of longer linear nanoparticle chains, ultimately demonstrating the practicality of the dimer configuration over more complex nanostructures.

ACKNOWLEDGMENTS

There are many people I owe thanks to for their help in getting this document prepared and, perhaps more importantly, making sure the process of doing so didn't destroy my sanity in the process. First, I should thank my advisor, Dr. Rene Lopez, whose mentoring style helped me to forge a sense of confidence and independence as a researcher over my 6 year tenure at UNC. I would also like to thank the members of my entire committee, Laurie McNeil, Richard Superfine, Royce Murray and Chuck Evans for their time, attention, and helpful suggestions throughout the course of this project.

It is a known fact that this project wouldn't have gotten off the ground if not for inordinate amount of help that was received from a number of very generous collaborators. Professor Hongxing Xu ranks among the most important of these benefactors, whose offer to use the facilities in his lab on two occasions (one of which he financed independently) provided a critical means of gathering the data on which this thesis is based. Another collaborator, Dr. Angela High Walker of NIST generously funded a visit to her lab to gather information on the nanochain portion of this thesis using an instrument not yet available on the UNC campus. Dr. Kwan Skinner, also played an important role in the development of the nanorod dimers that were used in the interparticle gap experiments. Finally, much of the scope and creative element of this project found its way to promi-

nence in the form of many useful conversations with Prof. Rich Superfine, without whose wide reaching understanding of physics as a niche discipline in the gargantuan field of science as a whole, the idea for the experiments with elastomers would never have been hatched.

For my sanity, I owe many thanks to Jorge Cham (Piled High and Deeper) and Randall Munroe (XKCD). Your work provided comic relief as well as a sense of reassurance that I had not, in fact, entered the Twilight Zone when I started graduate school. Along similar lines, I also owe thanks to the Trailheads, who were like family: You provided a much-needed means of creating balance to a difficult lifestyle. I will never forget post-run mornings at the Open Eye, the kilts, Uwharrie and loads of other things I don't have space to mention here. Finally, I should thank a group of guys named Steven Tyler, Joe Perry, Tom Hamilton, Brad Whitford, and Joey Kramer. Both your story and your music has inspired and sustained me since I first annoyed my parents with my purchase of *Pandora's Box* back in 1991. You may be happy (or horrified) to know that the majority of this thesis was written to the sound of *Permanent Vacation*, *Pump*, and *Get a Grip* blaring out of a set of headphones. Thanks for your part in leading me to the last few keystrokes of this document.

Last, but certainly not least, I owe a heartfelt thanks to my family. Thank you, mom, dad, Jim and Lynda, who taught me the importance of finishing the things I chose to start. To the Martin family, who treated me like a daughter and sister before I actually was. To Andypants, who taught me the importance of irreverence, as only a dog can truly show you. Finally, I owe thanks to my husband Kevin Martin, for agreeing to

move 2,500 miles away from family and friends and putting up with six years of graduate school-induced madness to boot. You have been my rock when the ardor of this journey threatened to make me forget who I was and why I was here - I love you more than I will ever be able to say. With you by my side I know that everything is going to be just fine, fine, fine...

Contents

List of Abbreviations

AAO	Anodic aluminum oxide
AFM	Atomic force microscopy
Al	Aluminum
Au	Gold
C	Coulomb
CCD	Charge-coupled device
Cr	Chromium
Cu	Copper
cw	Continuous wave
DFT	Density functional theory
EF	Enhancement factor
FDTD	Finite-difference Time-domain method
FEM	Finite Element Method
FIB	Focused ion beam
FIT	Finite integral technique
Ga	Gallium
GMT	Generalized Mie Theory
Li	Lithium
LMIS	Liquid-metal ion source

LSPR	Localized surface plasmon resonance
NIL	Nanoimprint lithography
NP	Nanoparticle
OD	Optical density
Pd	Palladium
PDMS	Poly(dimethylsiloxane)
PFPE	Perfluoropolyether
PLGA	poly(lactic-co-glycolic acid)
PRINT	Pattern Replication in Non-wetting Templates
Pt	Platinum
SEM	Scanning electron micrograph/microscopy
SERS	Surface-enhanced Raman spectroscopy/scattering
SiO_2	Silicon dioxide
SSEF	Surface-averaged SERS enhancement factor
SPP	Surface plasmon polariton
TE	Thermo-electric
UV	Ultraviolet

List of Symbols

ϵ_0	Permittivity of free space
ϵ_M	Permittivity of embedding medium
λ	wavelength
Ω	Solid angle
ω	frequency
c	Analyte concentration
G	Surface enhancement factor
$\mathbf{I}$	Intensity
L	Length
n	Index of refraction
N_A	Avogadro's number
P	Power
$\mathbf{V}$	Voltage
V	Volume
$\mathbf{W}$	Watt

List of Figures

There is a theory which states that if ever anybody discovers exactly what the Universe is for and why it is here, it will instantly disappear and be replaced by something even more bizarre and inexplicable. There is another theory which states that this has already happened.

-Douglas Adams

English humorist & science fiction novelist (1952 - 2001)

Chapter 1

Introduction

I was born not knowing and have had only a little time to change that here and there.

-Richard P. Feynman

1.1 Overview

The integration of surface-enhanced sensing techniques into various chemical sensing technologies is a matter of increasing scientific as well as societal interest. The application of surface-enhanced Raman spectroscopy (SERS) to chemical sensors with the ability to detect substances at the single molecule level [33, 51, 86] stands to benefit a broad range of fields and is currently receiving a great deal of attention from researchers. Specifically, SERS can potentially provide a means of unambiguously identifying target substances at the trace level - an ability that, if correctly developed and applied, could dramatically improve the function of chemical sensors used in a gamut of settings.

However, the development of such technologies necessitates a thorough understanding of the SERS effect, including the mechanisms from which the SERS enhancement arises as

well as logistical barriers and short-comings of current fabrication techniques that stand in the way of the development of highly-efficient SERS-active sensors. A great deal of progress has been made, especially on the theoretical front, since its discovery in 1977 [25]. However, the experimental testing of these theories has been severely hampered by low-throughput fabrication techniques and enhancement factor reproducibility issues. This dissertation presents efforts towards solving these problems in form of novel experimental approaches to both the fabrication of SERS-active substrates and the measurement of the SERS enhancement factor.

1.2 Raman Spectroscopy

1.2.1 Introduction

Originally observed in 1921 by its namesake, Sir Chandrasekhara Venkata Raman [63] (who subsequently won the 1930 Nobel prize in physics for this discovery), Raman scattering is a two-photon inelastic scattering process that can be used to identify symmetric modes in a system. When monochromatic light impinges on a molecule, most of the light is elastically (Rayleigh) scattered. However, a small number of photons interact with the electron cloud and the molecular bonds, thereby raising the molecule to an excited virtual state. When the molecule drops back down to a lower vibrational state, it emits a photon of a different energy than that of the source beam. The difference between these two energies is known as the *Raman shift* and is written as $\Delta E_{\mathrm{R}} = E_{\mathrm{L}} - E_{\mathrm{S}}$ where E_{L} and E_{S} are energies of the source (usually a laser) and the scattered photons, respectively.

These differences in energy correspond to the intrinsic vibrational modes in molecules, forming the basis for the Raman spectrum which helps to identify the atomic orientation and bonding within a system.

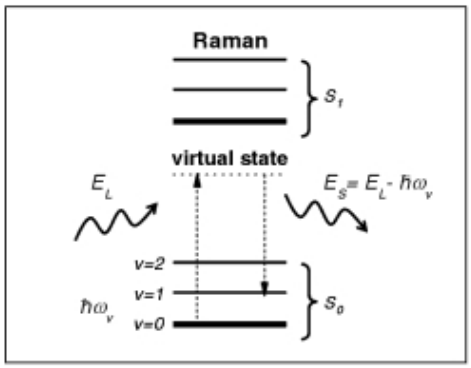

Figure 1.1: Simplified schematic Jablonski diagram illustrating the Raman processes. If the emitted photon is less energetic than the source beam (indicating that some of its initial energy was"left behind" as vibrational energy in the molecule), the photon is said to be Stokes scattered. Conversely, if the photon interacts with a molecule that is already in an excited virtual state, it is possible for the scattered photon to emerge with more energy than the incident beam. This case is called Anti-Stokes scattering [37].

Raman spectroscopy finds itself in the company of a wide variety of optical spectroscopies. However, the technique to which it is constantly being compared is fluorescence spectroscopy. Fluorescence spectroscopy is primarily concerned with the electronic and vibrational energy states in molecules. Specifically, the molecule of interest is excited from one electronic energy state to another. It then relaxes through the various vibrational states until it reaches the bottom of the excited state, where it then returns to the ground state and emits a photon. Because the photon may travel through any number of vibrational states on its path back to the ground state, photons that are emitted show a wide range of frequencies, which is often used to determine the structure of vibrational states in molecules. While fluorescence spectroscopy has the advantage of a large

cross-section, it suffers from photobleaching and, perhaps more importantly, the broad absorption peaks which make identification of unknown substances more difficult when compared to the narrow-peaked, fingerprint-like Raman spectra (a topic that will be discussed further in the following sections). It is in these areas that Raman spectroscopy offers a viable alternative to such well established techniques.

Finally, it is important to note that when Chandrasekhara Raman made the first Raman measurement, he used only color-filtered sunlight as his source and his eyes as his detector. Due to the rudimentary nature of optical setups at the time, practical applications of Raman spectroscopy in common lab settings were uncommon and advances in the technique languished for many years. Fortunately, the advent of laser and advanced photon detection technologies has renewed interested in Raman spectroscopy as a practical optical spectroscopic technique. As a testament to this renewed interest, in a recent paper published by W. Kiefer [32] over 300 references of key developments published in the *Journal of Raman Spectroscopy* alone over the past few years are listed. These advances exist in a broad range of fields, including but not limited to art and archaeology, forensic science, solid state physics and the biosciences, demonstrating the increasing relevance of Raman spectroscopy as a useful investigative tool in science and the clear benefits of continued advancements in its application to practical problems.

1.2.2 Formal Definition of the Raman process

Quantum Theory

The fully classical approach to Raman scattering (which will be described in detail in the next subsection) is sufficient in most cases, providing a means of explaining the link between polarizability and molecular vibrational modes and their connection to symmetries and selection rules. However, for the sake of completeness, the Raman process relies heavily on quantum mechanics to quantitatively link the Raman polarizability to the microscopic properties of the molecule. Thus, a quantum mechanical approach is needed to: (a) fully justify the classical approach and, (b) provide a means of dealing with the few situations in which the classical approach fails. Specifically, processes such as spontaneous Stokes scattering and the zero-point amplitudes of molecular modal oscillations complete the link between the Raman cross-section and the microscopic properties of normal modes - a link that is of critical importance for the understanding of resonant Raman scattering as well as the correct interpretation of the results of Raman Density Functional Theory (DFT) calculations [37]. However, the classical approach in terms of the ability to describe the Raman polarizability is all that is needed to develop the argument in the case of surface-enhanced Raman spectroscopy (SERS), precluding the need for a detailed description of the quantum approach here.

Classical Theory

Raman scattering occurs as a result of oscillations of the induced electronic dipole moment when a molecule is exposed to an oscillating electric field. This dipole moment

forms the basis for calculating other aspects of Raman radiation, including the power emitted per unit solid angle (i.e. the radiation profile) and the Raman cross-section. For a dipole $\mathbf{p}(\omega) = p\mathbf{e}_z \sin \omega t$ embedded in a medium with index of refraction $n_{\mathrm{M}} = 1$ the radiation profile is given as [23]:

$$\frac{dP_{\mathrm{Rad}}}{d\Omega}(\Omega) = \frac{w^4}{32\pi^2\epsilon_0 c^3}|\mathbf{p}|^2 \sin^2\theta \tag{1.1}$$

Where ω, ϵ_0, c, and Ω are the frequency of the incident radiation, the permittivity of free space, the speed of light and the solid angle, respectively. Here, it is important to note that because most dipoles encountered in common experimental settings are not in a perfect vacuum and the detecting optics do not detect radiation emitted from all angles, the total power radiated should be obtained by integrating over a solid angle accurately reflecting the geometry of the sample and detection setup.

Here, it is important to highlight the fact that the process that couples photons to the vibrational modes of a molecule is inherently governed by quantum mechanics. However, this process can be reduced to a classical approach where the Raman polarizability carries the quantum mechanical information that ultimately relates ω_{L} and ω_{R}. Using the classical description, we begin with the excitation source, a monochromatic light beam oscillating at angular frequency ω_{L} with wavevector $\mathbf{k}_{\mathrm{L}}$:

$$\mathbf{E}(\mathbf{r}, t) = \mathbf{E}(\mathbf{k}_{\mathrm{L}}, \omega_{\mathrm{L}}) \cos(\mathbf{k}_{\mathrm{L}} \cdot \mathbf{r} - \omega_{\mathrm{L}} t) \tag{1.2}$$

For a specific vibrational mode of energy $\hbar\omega_{\mathrm{v}}$, the Raman scattered radiation is at a

frequency $\omega_{\mathrm{R}} = \omega_{\mathrm{L}} - \omega_{\mathrm{v}}$. The sinusoidal oscillation of the incident radiation induces a Raman dipole, $\mathbf{p}_{\mathrm{R}}(\omega_R)$ which must therefore oscillate at frequency ω_{R}. This allows us to represent the Raman polarizability tensor, $\hat{\alpha}_{\mathrm{R}}(\omega_{\mathrm{L}}, \omega_{\mathrm{v}})$ for a given vibrational mode as:

$$\mathbf{p}_{\mathrm{R}}(\omega_{\mathrm{R}}) = \hat{\alpha}_{\mathrm{R}}(\omega_{\mathrm{L}}, \omega_{\mathrm{v}}) \cdot \mathbf{E}(\omega_{\mathrm{L}}) \tag{1.3}$$

where $\hat{\alpha}_{\mathrm{R}}(\omega_{\mathrm{L}}, \omega_{\mathrm{v}})$ is of critical importance as it helps to define the relationship between $\mathbf{p}$ and $\mathbf{E}$ (See appendix A for a detailed explanation of the Raman polarizability tensor).

Here, it is important to point out that the macroscopic electromagnetic fields (i.e. the fields averaged over a small volume) and the microscopic fields (i.e. the fields localized at the molecular or atomic level) are two different entities. Microscopic fields are often more complicated in nature than macroscopic fields and, as they are what is predominantly felt by the molecule of interest, they are what should be used to describe the Raman dipole.

The difference between macroscopic and microscopic fields is addressed using the local field correction, L_{M}. Here, the microscopic electric field is related to the macroscopic electric field using the following relation:

$$\mathbf{E}_{\mathrm{Micro}} = (L_{\mathrm{M}})^{1/4} \mathbf{E}_{\mathrm{Macro}} \tag{1.4}$$

where $(L_{\mathrm{M}})^{1/4}$ is expressed as:

$$(L_{\mathrm{M}})^{1/4} = \frac{n_{\mathrm{M}}^2 + 2}{3} = \frac{\epsilon_{\mathrm{M}} + 2}{3} \tag{1.5}$$

and n_{M} and ϵ_{M} are the index of refraction and the permittivity of the embedding medium, respectively (see Appendix B for a more detailed definition of the origin of L_{M}). Combining this with the Raman polarizability tensor, the local field corrected relationship between $\mathbf{p}$ and $\mathbf{E}$ can be defined as follows:

$$\mathbf{p}_{\mathrm{R}}(\omega_{\mathrm{R}}) = (L_{\mathrm{M}})^{1/4}\hat{\alpha}_{\mathrm{R}}(\omega_{\mathrm{L}}, \omega_{\mathrm{v}}) \cdot \mathbf{E}(\omega_{\mathrm{L}}) \tag{1.6}$$

This can now be substituted into equation 1.1 to give a differential scattered power in the 90° configuration (i.e. in the commonly used back-scattering configuration where the incident and detected beams are along the same direction) as:

$$\frac{dP_{\mathrm{Rad}}}{d\Omega}(\theta = 90^{\circ}) = \frac{\omega_{\mathrm{R}}^4 n_{\mathrm{M}}}{32\pi^2\epsilon_0 c^3} L_{\mathrm{M}} |\alpha|^2 |\mathbf{E}_{\mathrm{Inc}}|^2 \tag{1.7}$$

which can be integrated over the relevant solid angle to give the power radiated by the Raman dipole.

1.3 Introduction to plasmonics

The formal definition of a plasmon is given as "a quantum quasi-particle representing the elementary excitations, or modes, of the charge density of a plasma" [58]. In short, this refers to the fact that metals possess a sea of free electrons that are highly mobile and can, consequently, be driven at a resonance frequency to support highly enhanced electromagnetic fields which form the rock upon which surface-enhanced Raman spectroscopy is based.

A range of plasmons have been identified, corresponding to the multitude of different media that support them. In the case a perfect infinite thin metallic film, electronic oscillations can propagate forever across the surface, giving rise to the surface plasmon polariton (SPP). However, in the case of the nanoparticles used in this thesis, their small size gives these ripples in the electronic media nowhere to travel. In this particular situation, small nanoparticles exhibit localized surface plasmon resonances (LSPRs), corresponding to the oscillatory displacement of the electrons in a metallic nanoparticle from the heavier ionic core.

The long-wave approximation presents a simple solution that retains key features of localized plasmon excitations in metal nanoparticles. For example, let us consider a metallic sphere much smaller than the wavelength of the incident beam and embedded in a dielectric medium of permittivity ϵ_{M} and solve the problem using the electrostatic approximation (see section 1.4.3). The complex electric field inside the sphere can be shown to be constant and proportional to:

$$E_{\mathrm{In}} = \frac{3\epsilon_{\mathrm{M}}}{\epsilon(\omega) + 2\epsilon_{\mathrm{M}}} E_0 \tag{1.8}$$

The important part of this expression is the denominator which, if it were 0, would result in a divergence in the internal electric field. This is not possible for standard dielectrics, for which ϵ_{M} is typically between 1 and $\sim$ 10. However, in metals, this condition can nearly be met if the absorption is small $\mathrm{Im}(\epsilon(\omega)) \ll -2$ at a wavelength where $\mathrm{Re}(\epsilon(\omega)) \sim -2\epsilon_{\mathrm{M}}$. This reduces the problem to a simple assessment of which laser lines and metals are appropriate for the given measurements, bringing us to the question

of "which metals are good for plasmonics and SERS?". This can be answered simply by looking closely at equation 1.8, from which the following conditions are derived: (1) Re(ϵ) *must* be negative in the wavelength of interest and (2) Im(ϵ) *must* simultaneously be small in the same wavelength range. Taking this information into consideration, this narrows the number of a truly useful metals for SERS significantly.

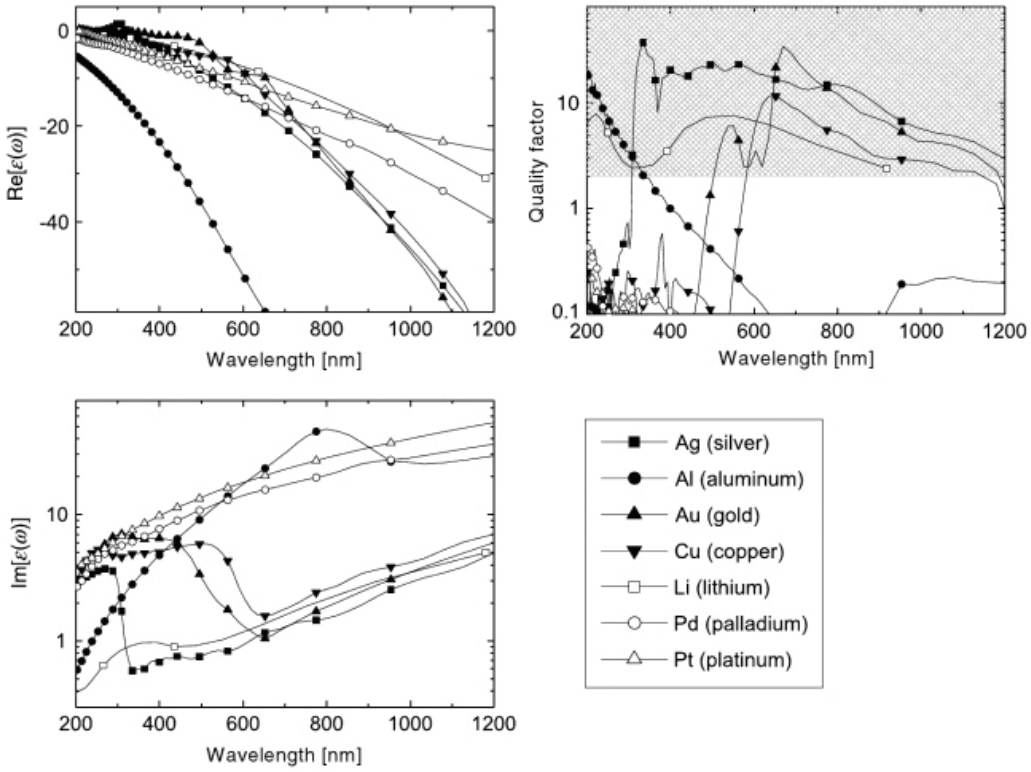

Figure 1.2: Overview of the optical properties of a selection of metals in the (extended) visible range. The real (top) and imaginary (bottom) parts of ϵ are plotted against wavelength on the left. Also shown (top-right) is the predicted approximate quality factor Q of the localized surface plasmon resonances for a metal/air nano-particle. The shaded area is the area of interest to many plasmonic applications. [37]

From the examples in Fig. 1.2, it is clear that Al, Pt and Pd exhibit too much absorption in the visible range while Al would only be of use in the ultraviolet spectral region. Au an Cu are seem to exhibit the necessary properties, but only at the higher

end of the visible spectrum (∼600 nm) while Ag performs best at wavelengths around ∼400 nm. Li also exhibits suitable properties, but only in the far infrared region.

In experimental settings, it is clearly necessary to take into account factors such as cost, durability, toxicity, availability and ease of integration into experiments. For these reasons, Au and Ag are the most commonly used metals for SERS applications - Au because it does not readily tarnish or oxidize under normal laboratory conditions and Ag because of its ability to produce the highest enhancement factors. Due to the fact that the tarnishing of a Ag substrate [44] would adversely affect the outcome of the experiments performed in this project, Au was the metal of choice for all experiments described in this dissertation.

Finally, it is of critical importance to describe the plasmonic interaction that occurs when two nanoparticles are brought very close together (typically, within the range of 1-5 nm). This effect, termed the gap surface plasmon polariton, is the result of the interaction of the localized surface plasmon modes of two distinct nanoparticles. This interaction produces hybridized modes and can create large local enhancements in the few nanometers of volume between the two nanostructures. This effect, which forms the basis for SERS in closely spaced nanoparticle pairs, is of critical importance in explaining the dimer enhancement, which will be described in detail in section 1.5.

1.4 Introduction to Surface-enhanced Raman Spectroscopy (SERS)

Raman scattering is, by nature, an extremely weak process (e.g. only about 1 photon out of every 10^7 incident photons is Raman scattered) [37]. However, Raman spectra typically have narrow, well defined peaks, giving them a "fingerprint-like" quality that is extremely useful for unambiguously identifying molecules. This, coupled with the fact that Raman scattering, unlike commonly used fluorescence spectroscopy techniques, is resistant to photobleaching, renders its continued investigation and application-based improvement a topic of intense interest.

In 1977, Richard Van Duyne and David Jeanmaire discovered that they could achieve enormous enhancements of the Raman signal when the target molecules were brought within the vicinity of an electrochemically roughened silver substrate [25]. This approach, eventually termed surface-enhanced Raman scattering (SERS), arises from a mutual resonance between the locally large Raman electromagnetic fields and a molecule/molecules brought into close proximity of this enhanced area and has been found to produce enhancement factors anywhere from 10^6 to $10^{10} - 10^{13}$, depending on the experimental conditions.

In essence, the success of this particular experiment was auspicious. The SERS enhancement, which will be described in detail in the following subsection, is sensitive to a gamut of electromagnetic, chemical and morphological factors which must be considered in future experiments if the effect is to be well understood, controlled, and effectively

used in practical applications.

1.4.1 Definition of the SERS enhancement factors

In order to adequately preface the definition of the SERS enhancements factors (EFs), it is necessary to state the factors currently known to have a significant effect on the strength of the total enhancement. The SERS process (and, therefore, the enhancement factor) depends on the ability to control specific factors, including:

- *Characteristics of the laser excitation.* In particular, this includes the wavelength, intensity, angle of incidence and polarization of the incident beam with respect to the substrate.

- *Detection setup.* Specifically, this refers to the scattering configuration (e.g. backscattering geometry), solid angle for collection and polarized/unpolarized detection.

- *SERS substrate.* Of importance here is the material used, the refractive index, n_{M}, of the medium in which it is embedded, the orientation of the substrate with respect to the polarization of incident light, and whether the substrate is a planar surface (2-D) or in solution (3-D).

- *Intrinsic properties of the analyte.* Specifically, the Raman cross-section (i.e. the ability to inelastically scatter photons) of the molecule to be probed.

- *Analyte adsorption properties*, in particular, the ability of a large quantity of the target molecule to be brought into close proximity of the enhanced area of the

substrate will invariably increase the Raman signal for a given experiment. The orientation of the molecules with respect to the surface is also important, as the tendency towards fixed or random orientations influences surface selection rules that can drastically modify the total Raman enhancement. Finally, if the molecule is capable of being chemically adsorbed, the subsequent modification of the molecule forms the basis for the chemical contribution to the enhancement (described in detail in section 1.4.5).

Clearly, it is not possible to meet or control all of these criteria simultaneously in an experimental setting nor it is always necessary to do so. It is important, however, to note that the sheer sensitivity of the SERS EF to the parameters listed above make the local field enhancement strongly dependent on the exact position of the molecule with respect to the surface. As a result, the SERS EF for typical SERS substrates are *highly non-uniform*. Thus, it is necessary to be careful in the crafting as well as the application of a mathematical definition of the SERS EF to experiments conducted in the lab. For this reason, two types of SERS enhancement factors have been defined, each of which is specifically designed to adequately assess the two main EFs of current scientific interest: the surface-averaged EF of a substrate and the single-molecule EF at a specific position on a substrate. All experimental assessments of the SERS EF in the experiments described in this dissertation fall into the category of "surface-averaged", so a formal definition of the surface-averaged SERS EF (SSEF) is provided in the following sections.

The chemical enhancement

Although it is generally believed that electromagnetic effects are responsible for the bulk of the enhancements in SERS, the existence of an additional mechanism termed the 'chemical enhancement' is also believed to play a role in boosting the Raman signal. Unfortunately, the exact definition of what the chemical enhancement is exactly has long been a matter of debate. Not only has it proven difficult to measure experimentally but also:

"... the magnitude of this effect rarely exceeds a factor or $\sim$10, and is best thought to arise from the modification of the Raman polarizability tensor of the adsorbate, resulting from the formation of a complex between the adsorbate and the metal. Rather than an enhancement mechanism, the chemical effect is more logically to be regarded as a change in the nature and identity of the adsorbate." [46]

Taking this view, one arrives at the position that the 'chemical enhancement' corresponds to the modification of the Raman polarizability of a molecule when it is adsorbed onto a metallic surface. A detailed discussion of this effect can be found in Ref [46]. However, since the effect is generally very small, only a short overview of the charge transfer mechanism - the most studied mechanism for the chemical enhancement - will be included here.

The charge transfer mechanism, in short, is based on the idea that the interaction between metallic surfaces and the electrons in molecules can force the molecules into a state that has a higher Raman cross section. There are two main ways this is believed to occur [55, 73]:

- Situation 1 describes the most simple of situations in which the molecule does not bond covalently with the metallic surface. In this case, the proximity of the metal serves to perturb the electronic structure of the molecule, thereby modifying the polarizability in a way that could potentially increase the Raman efficiency of a particular mode. It is important to note here, however, that this effect does not always improve the Raman signal. As it merely *interferes* with the natural electronic structure of the molecule, it has just as much potential to quench the signal as it does to enhance it.

- Situation 2 involves the covalent bonding of the analyte to the surface of the metal. The binding of the molecule to the metal has a direct and often significant effect on the intrinsic polarizability of the molecule. Polarizability depends explicitly on the availability of certain optical transitions which can be provided (indirectly) by the overlapping of molecular orbitals. Furthermore, it is also possible that the surface complex can create a new electronic state that is close to or actually in resonance with excitation source. In the latter case, the chemical enhancement is actually a resonant-Raman enhancement.

In essence, while there is little debate that the chemical enhancement plays a role in total SERS enhancement, the effect is still poorly understood and its contributions are, thus, difficult to determine. Furthermore, because it has been well established that the electromagnetic enhancement is the dominant portion of the total SERS enhancement factor, this will become the effect focused on in all experiments described in this dissertation.

Surface-averaged SERS Enhancement Factor (SSEF)

For large areas involving a large number of molecules adsorbed to the substrate, it makes sense to define an average SERS EF (also known as the SERS substrate enhancement factor or SSEF) for the entire area measured. For this, this following relation can be used:

$$SSEF = \frac{I_{\mathrm{SERS}}/N_{\mathrm{Surf}}}{I_{\mathrm{RS}}/N_{\mathrm{Vol}}} \tag{1.9}$$

where $N_{\mathrm{Vol}} = c_{\mathrm{RS}}V$ is the average number of molecules in the scattering volume, V, for analyte concentration c_{RS} in the Raman (not SERS) measurement, producing Raman signal intensity I_{RS}. N_{Surf} is the average number of *adsorbed* molecules in an identical scattering volume for SERS experiments, producing Raman signal intensity I_{SERS}. In essence, this ratio is simply an average over all possible molecular orientations, providing a means of circumventing the non-uniformity problem for SERS measurements of an analyte monolayer. This expression has been well established [6] and is usually considered to be the best estimate of the average SERS EF over the surface of a given substrate.

1.4.2 Overview of the main EM effects in SERS

Local field enhancement

As mentioned back in section 1.2.2 in the explanation of the classical approach to the Raman process, the macro- and microscopic electromagnetic fields are not usually the same. In the case of SERS, the electromagnetic fields are strongly modified in the

vicinity of metallic objects. Effectively, this means that the local electric field ($\mathbf{E}_{Loc}$) at a molecule can be completely different in strength as well as orientation to that of the incident beam ($\mathbf{E}_{\mathrm{Inc}}$). This is relevant to SERS in the sense that $|\mathbf{E}_{\mathrm{Loc}}|$ on a metallic surface can be *much larger* than $|\mathbf{E}_{\mathrm{Inc}}|$, especially in specific localized positions referred to as 'hot spots'. The local field induces a Raman dipole $\mathbf{p}_{\mathrm{R}} = \alpha_{\mathrm{R}}\mathbf{E}_{\mathrm{Loc}}(\omega_{\mathrm{L}})$ which is subsequently enhanced by a factor of $|\mathbf{E}_{\mathrm{Loc}}(\omega_{\mathrm{L}})|/|\mathbf{E}_{\mathrm{Inc}}|$. If this induced Raman dipole were to radiate in free space, the amount of energy radiated would be enhanced by a factor of:

$$M_{\mathrm{Loc}}(\omega_{\mathrm{L}}) = \frac{|\mathbf{E}_{\mathrm{Loc}}(\omega_{\mathrm{L}})|^2}{|\mathbf{E}_{\mathrm{Inc}}|^2} \tag{1.10}$$

which is referred to as the local field intensity enhancement factor.

Radiation enhancement

In a typical SERS configuration, the Raman dipole radiates in close proximity to a metal. These radiated fields are strongly affected by the metal in a manner almost identical to that of the excitation field. The substrate onto which the molecule is absorbed affects the total power radiated predominantly in the two following ways:

- Clearly, the presence of the substrate affects the *radiation pattern* of the power emitted into the far field (i.e. $dP_{\mathrm{Rad}}/d\Omega$) through the simple act of "being in the way". For example, the presence of a flat metallic surface close to a radiating dipole has the capacity to block half of the power that would otherwise be emitted into the far field by a dipole in free space.

- The *total radiated power* (i.e P_{Rad}) by a dipole can be largely quenched or, equivalently, boosted compared to that of the same dipole in free space, P_0, as a result of the presence of the metallic substrate. Specifically, this means that, for a given fixed oscillating dipole of amplitude P_0, more or less energy will be extracted from this dipole depending on the electromagnetic environment. Here, it is important to make note of two important points: (1) This effect is the result of the emission process itself being directly affected by the metallic environment. More importantly, it does not mean (and it is wrong to think) that the molecule is radiating into free space and the emitted field is subsequently being enhanced by the local electromagnetic environment, as the origin of SERS is so often simplified. (2) This process does not contradict energy conservation since an external source of energy (i.e. the laser beam) is present to maintain the amplitude of the dipole.

Taking the aforementioned information into consideration, the radiation enhancement factor can therefore be defined as $M_{\mathrm{Rad}} = P_{\mathrm{Rad}}/P_0$.

1.4.3 The common $|E|^4$-approximation to SERS enhancements

In the event that only two main mechanisms of enhancement (namely, the local and radiative field enhancements) are considered, the SERS EF can be simplified to the following expression:

$$EF_{\mathrm{SERS}} \approx \frac{|\mathbf{E}_{\mathrm{Loc}}(\omega_{\mathrm{L}})|^2}{|E_{\mathrm{inc}}|^2} \frac{|\mathbf{E}_{\mathrm{Loc}}(\omega_{\mathrm{R}})|^2}{|E_{\mathrm{inc}}|^2} \tag{1.11}$$

This expression provides and fairly simple way *estimating* the SERS EF if the local field and Raman frequencies are known. Moreover, in many cases, the Raman shift is small, allowing for the further approximation that $\omega_{\mathrm{R}} \approx \omega_{\mathrm{L}}$. This produces the famous zero-Stokes shift $|E|^4$-*approximation*, which is expressed as:

$$EF_{\mathrm{SERS}} \approx \frac{|\mathbf{E}_{\mathrm{Loc}}(\omega_{\mathrm{L}})|^4}{|E_{\mathrm{Inc}}|^4} \tag{1.12}$$

The above equation is commonly considered to be one of the more important equations in SERS research and is the approximation that is applied to all experimental sections of this dissertation.

Calculation of the SERS EF under typical experimental conditions

One of the problems that has plagued the advancement of SERS-related research on the experimental front is the gulf that exists between theoretical models and actual samples created in the laboratory. The SERS EF, as will be explained in greater detail in the following sections of this dissertation, is very sensitive to minute morphological factors at hot spots. This leads to highly non-uniform results and, perhaps more importantly, irreproducible EFs across the area of a single sample. Consequently, it is important to realize that although the formal description of the SERS EF is entirely consistent, it does not account for small irregularities in substrate shape, roughness, molecular orientation, packing density, etc. that are responsible for wide variations in the enhancement. For this reason, one must be careful when applying these equations in the calculation of 'real life' SERS EFs. Not only must researchers be cognizant of what these equations represent,

they must also be aware of the limitations of their knowledge regarding their sample. As such, if a uniform enhancement is desired over a large-area sample , the researcher *must* devise a way to control all parameters to which the SERS EF is sensitive (a feat that has yet to be realized due to the limitations of current fabrication techniques). Likewise, if the dependence of the SERS EF on a specific parameter is desired, the researcher must devise a way to hold all *other* parameters (save the one to be measured) constant. With regard to the dependence of the SERS EF on interparticle distance, this has been accomplished for metal nanoparticle dimers and a full description of this experiment is provided in chapter 5.

1.5 Metallic colloids and dimers

As previously mentioned, the surface roughness of the substrate plays a key factor in the ability to create 'hot spots' with large SERS EFs. Although researchers have discovered many nanoscale textured metallic surfaces capable of producing strong electromagnetic fields that give rise to SERS enhancements, metallic colloids and aggregates of such materials to some degree spell out the future of the development of many surface-enhanced techniques. Specifically, metallic colloids have provided an effective means of measuring the SERS EF of analytes in solution and, perhaps more importantly, 2-D aggregates of these colloids on the surface of a substrate have produced hot spots (irreproducibly, of course) exhibiting enhancement factors of 10^{10} or more, as quoted in the literature [43].

As mentioned in section 1.3, Au and Ag are the most commonly used metals in SERS experiments. Aside from beneficial properties of the bulk material from which they are made (see section 1.3), gold and silver colloids are also easily produced by well established reduction reactions. Gold colloids, in particular, are easily stabilized over a long period of time and the chemistry of molecular binding to gold (using thiol groups, for example) is well understood, lending to their widespread commercial availability and use. Citrate reduced colloids remain among the most widely used and are produced using the following method [50].

- 240 mg of $HAuCl_4$ is dissolved in 500 mL of distilled H_2O and brought to a boil.
- A solution of 1% sodium citrate (50 mL) is added during the boiling.
- The solution is left to boil for $\sim$ 1 h (with reflux), and subsequently cooled to room temperature.

Although aggregates of random numbers, sizes [35] and shapes[20] of nanoparticles have been studied and large enhancement factors reported [33, 86, 51], the dimer has persistently been shown to be an efficient SERS configuration. Along with the added benefit of being the most simple of all nanocluster configurations, it is this morphology upon which all of the experiments described in this dissertation are based.

Spherical nanoparticle dimers, in particular, possess a geometry that is particularly easy to theoretically model using the Generalized Mie theory (GMT) technique and the hottest 'hot spots' are always located in the interstices found directly between nanoparticle pairs. This fact, coupled with the ease at which these dimers can be experimentally

fabricated make the dimer a promising and potentially useful means of exploring the SERS phenomenon. For these reasons, the metal nanoparticle dimer has been the structure of choice for all experiments described henceforth.

Chapter 2

Experimental Techniques

There are children playing in the streets who could solve some of my top problems in physics, because they have modes of sensory perception that I lost long ago.

-J. Robert Oppenheimer

The purpose of this section is to provide an overview of all of the experimental techniques used in the work described in chapters 3-5 and is targeted at the reader who may be unfamiliar with some or all of these tools. For this expert reader, this chapter can be skipped altogether or simply referred back to on an as-needed basis.

2.1 Focused ion beam patterning

The focused ion beam (FIB), is an instrument commonly used in fields that require site-specific ablation and deposition at the micro- and nano- scale. Essentially, the FIB is a milling machine capable of ultra-fine precision, with many of the current models being capable of writing/milling features 15 nm or below. Most FIBs rely on a liquid-metal ion source (LMIS), generally gallium, which is placed onto a tungsten needle and

heated to its melting point. When the Ga melts, it wets the tungsten needle, creating an enormous electric field that both ionizes and accelerates the Ga ions away from the source. The ions are then accelerated through a potential difference of approximately 5-50 keV and focused into a beam by electrostatic lenses. When applied to a substrate, these high momentum ions literally knock atoms out of the substrate, enabling the precise patterning of substrates various made from a range of materials [34].

Most modern FIB systems also employ gas assisted etching through the chemisorption of reactive gasses on the substrate. One gas commonly used for this purpose is carbon tetrafluoride (CF_4). It is injected very near the area being sputtered and adsorbs onto atoms to be removed. This process of adsorption makes the substrate atoms volatile and force them to evaporate from the surface in a controlled manner.

2.2 High-throughput templating using PRINT

2.2.1 Nanoimprint Lithography (NIL)

Although many methods to recreate nanopatterns have surfaced over the years nanoimprint lithography (NIL) is special in is ability to rapidly create patterns over large surface areas in a reproducible fashion for a wide variety of materials. Generally, this technique is characterized by the use of a soft, elastomeric mold, typically poly(dimethylsiloxane) (PDMS), to either emboss or extrude structures on the nanometer or micrometer length scale [14, 77, 80, 79]. The relief pattern in the mold is generated by depositing a thin film of uncured PDMS onto a pre-patterned master (typically a silicon wafer), curing the

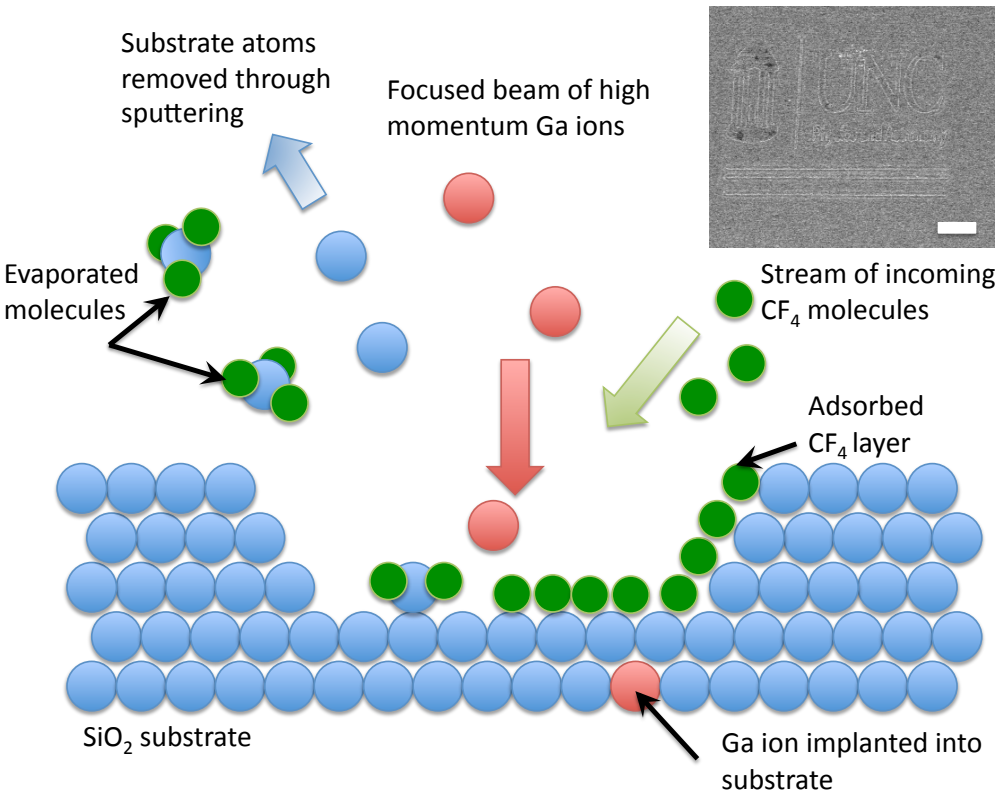

Figure 2.1: Schematic diagram of the FIB etching process. Inset: Example of the UNC logo etched into an SiO_2 substrate. Scale bar is 2 μm.

PDMS, then removing it to form a solid mold (Fig. 2.2). This mold is then brought into contact with the material to be patterned (e.g. photoresist, thermoplastic polymer, reactive monomer, etc.) and pressure is applied followed by the appropriate cure step. PDMS is a commonly used mold material based on its relatively low modulus and low surface energy which allow for a conformal contact and relatively easy release from the surface of the master and the patterned material. Furthermore, PDMS is transparent to UV light, making photocuring possible, if so desired/needed.

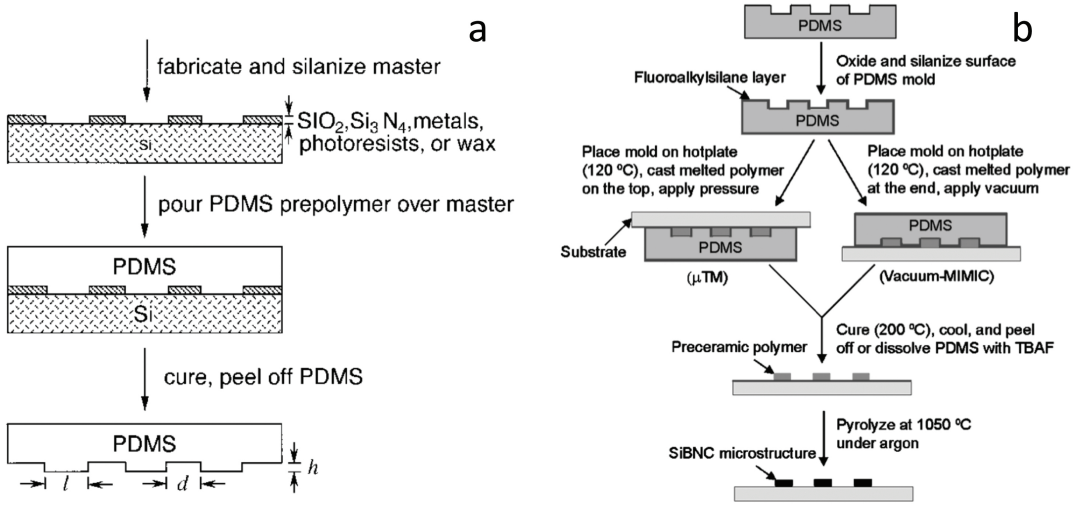

Figure 2.2: Schematic illustration of (a) the procedure for casting PDMS molds from a master having relief structures on its surface[80] and (b) procedures for fabrication of replica patterns using PDMS molds [89]

.

2.2.2 Pattern Replication in Non-wetting Templates (PRINT)

As mentioned above, PDMS has traditionally been used as a mold material for soft lithography. However, other elastomers have also been employed. One very special variety of elastomer that is used is perfluoropolyether (PFPE) and involves a technique

termed Pattern Replication in Non-wetting Template (PRINT). Developments involving this technique have been successful across a broad range of applications as it enables the fabrication of monodisperse particles and arrays of particles with simultaneous control over shape, size, composition and function [9, 42, 66, 17].

In Fig. 2.3, the capability of the PRINT process to create both isolated features as well as embossed films is illustrated. PFPEs belong to a versatile class of fluorinated polymers that have a number of advantageous properties: i) the PFPE liquid precursor has a very low interfacial tension, allowing features in a master too small to be replicated with a PDMS mold to be replicated.; ii) the PFPE precursor can be photochemically cured at room temperature to make a mold of the surface it has spread across; iii) once cured, the cross-linked, elastomeric PFPE material has a very low surface energy (8 - 10 dynes/cm) so can it be removed from the surface of the master without fouling it (a common problem with PDMS molds which limits the lifetime of expensive silicon masters). Furthermore, this technique can be expanded to large scale rollers, conveyer belt technology, or rapid stamping that allows for surface replication on the industrial scale.

2.3 Capillary force deposition

Capillary force deposition is a powerful technique that utilizes the forces associated with the meniscus of a solvent to assemble particles on a surface. Although many variants of this technique have been developed and successfully applied to problems in self-

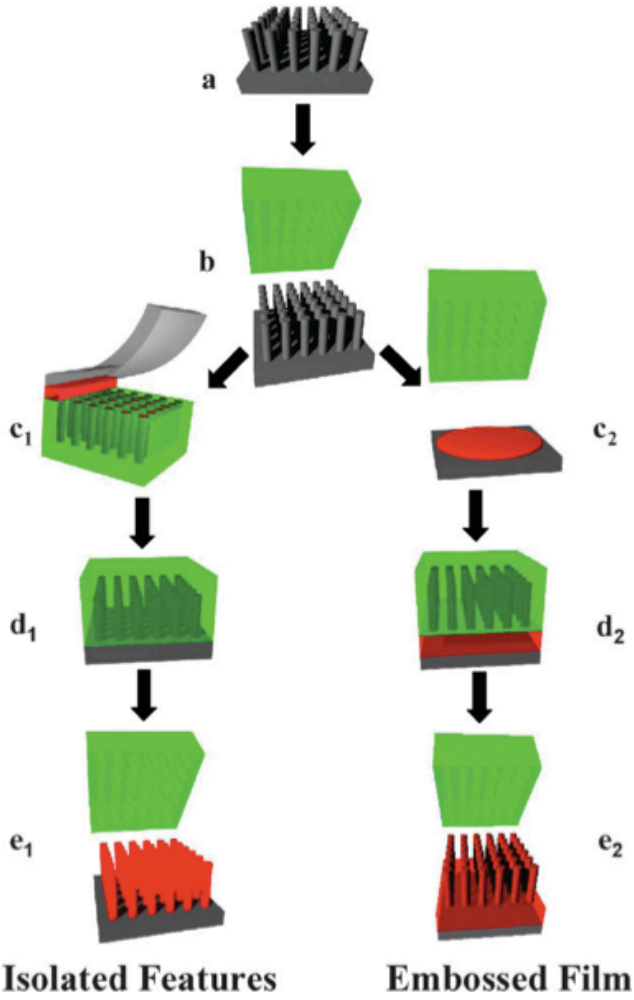

Figure 2.3: Schematic diagram of both isolated feature creation and film embossing. To create isolated features, a PFPE mold (b) is made of the features in a hard master (a). The polymer to be patterned is inserted into the mold (c_1) and a backing is applied (d_1) to support the particles. After curing, the mold is then peeled of yield a large-area array of identical polymer features. To create an embossed film, the polymer to be pattered in spread onto a support substrate (c_2). The PFPE mold is then applied to the surface, causing the polymer to wick up into the patterned area (d_2). After curing, the PFPE mold is peeled off, leaving an embossed film on a thin layer of residual polymer ("scum")

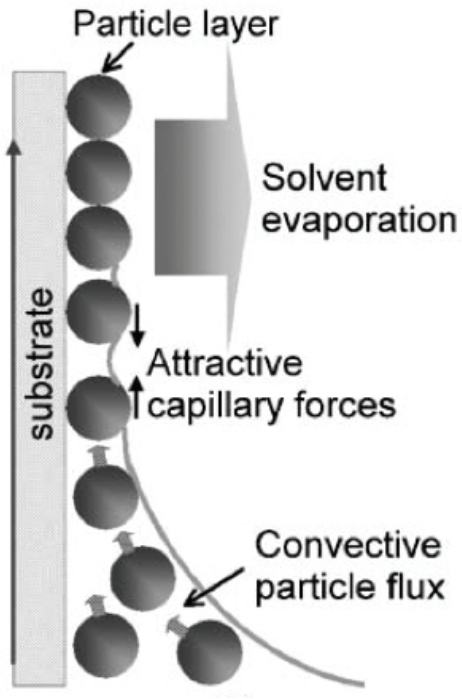

Figure 2.4: Schematic illustration of the mechanism of colloidal self-assembly in the vertical deposition technique in the case of 2D single layer colloidal arrays [8].

assembly [67, 7, 88, 81], the technique used in the experiments described in this dissertation involve an aqueous colloid suspended on a vertically oriented substrate. Deposition of the particles is a two part process. First, particles suspended in the colloid are directed to the three-phase contact line (i.e. the spot where the meniscus is pinned to the substrate) through a process termed particle convective flow. Particle convective flow is a process that occurs as a result of drag forces of the solvent moving in to replace the solvent that evaporated at the three-phase contact line and, most importantly, results in the flocculation of particles at this point. When the fluid level around the particle becomes comparable to the nanoparticle height, the solvent surface begins to deform. This deformation in conjunction with the natural surface tension of the liquid form the basis for the attractive interaction (i.e. the lateral capillary force) which ultimately draws the

nanoparticles together [49, 8].

In the most simple application of this technique, capillary force deposition can be used to deposit close-packed mono- and multilayers of particles onto a surface. However, if specific particle position is desired, this technique can be used on lithographically patterned templates which serve to control both the spacing and shape of the resultant nanoparticle aggregates. This technique was pioneered by Younan Xia [81, 88] who deposited sub-micron polystyrene beads into lithographically patterned glass (Fig. 2.5). This technique was later extended down to sub-100 nm nanostructures by Yi Cui *et al.* [7] who succeeded in patterning defect-free 50 nm and 60 nm metal nanoparticles on areas over 1000 μm^2.

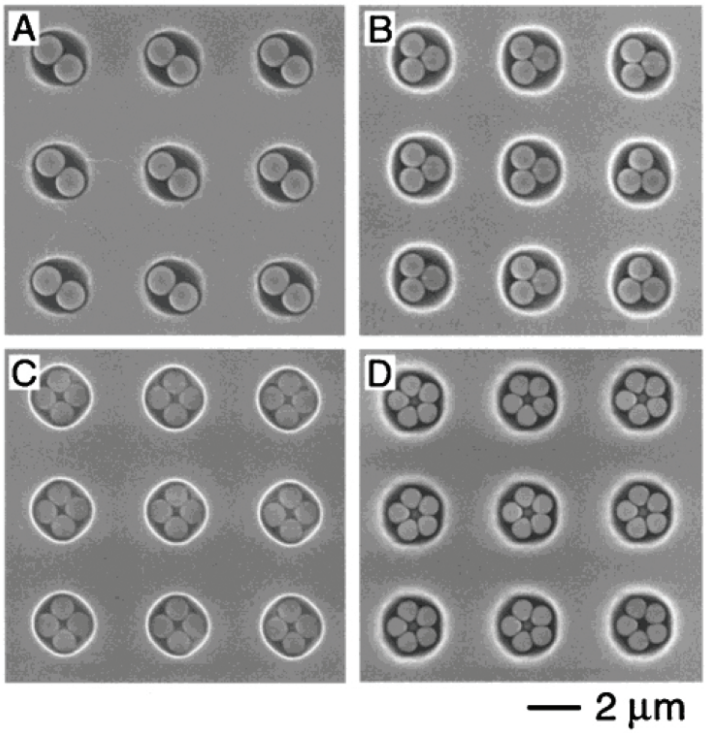

Figure 2.5: SEM micrographs of several typical examples of the self-assembled clusters: Single-layered units that include a) dimers; b) trimers; c) squares; and d) pentagons [88].

Here, it is important to point out that both Xia and Cui recognized the importance of the smoothness and wettability of substrate. In the case of thin film deposition, the a roughened and/or dirty surface interferes with the pinning of the meniscus. This fact becomes even more important when a lithographically patterned template is used in conjunction with small (e.g. < 60 nm particles). In this case, the capillary force F_c needs point in a specific angle to effectively direct the nanoparticles into the holes. In the experiments conducted by Cui *et al.*, it was discovered that optimum results could be achieved if the contact angle the solvent made with the substrate was between 10-30° [7]. These conditions can be achieved through the selection of compatible solvent/substrate material pairs, silane monolayer deposition, and keeping the substrate clean.

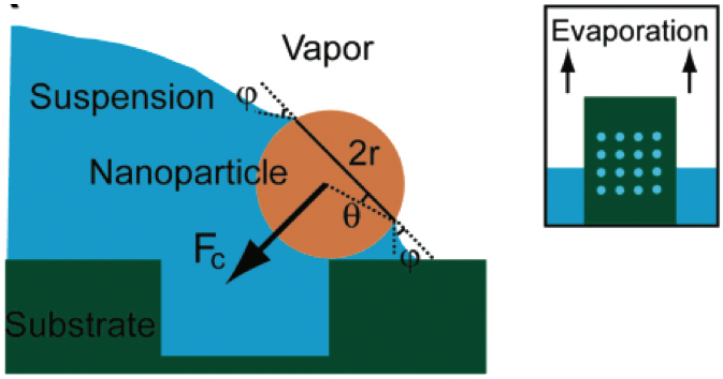

Figure 2.6: Schematic illustrating the capillary force (F_c) assembly mechanism at the vapor-suspension-substrate three-phase contact line (inset) Movement of the three-phase contact line is driven by evaporation by heating the solution to $\sim 60°$ C [7]

2.4 Reporter molecule functionalization of gold nanoparticles

2.4.1 Benzenethiol

In the testing of SERS-active structures, it is common practice to attach a probe/reporter molecule to the area of interest in order to gauge the strength of the enhancement factor. Usually, the molecules used for this purpose have high Raman cross-sections as it eases difficulties in achieving Raman signals with a high signal-to-noise ratio. Benzenethiol (also known as thiophenol or C_6H_5SH) is an organosulfur compound that is commonly used for this purpose. Thiophenol is the simplest of all of the aromatic thiols, which are characterized by sulfhydryl (-SH) end group and an aromatic ring.

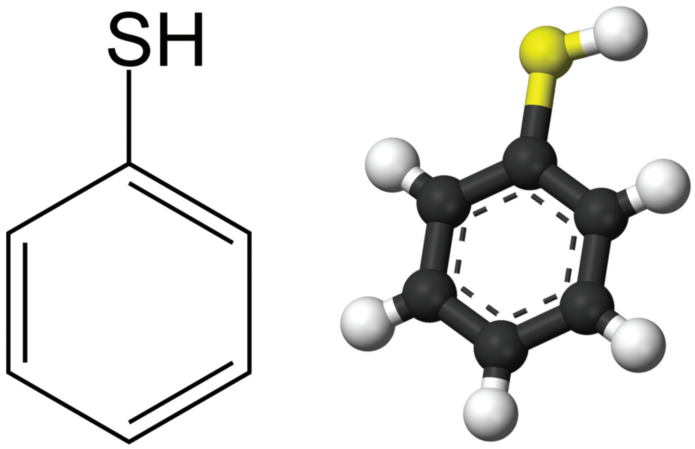

Figure 2.7: Two commonly used schematic representations of the benzenethiol molecule.

2.4.2 Solution-based functionalization of Au surfaces through capping agent-displacement

The benzenethiol molecule has a high affinity for gold due to the presence of sulfur in its end group. As such, it tends to displace other capping agents when it is adsorbed onto a gold surface and, afterwards, is not easily removed. This allows for the formation of self-assembled molecular monolayers of the reporter molecule that are both robust and in close contact with the gold surface (all important properties for creating large Raman signals as described in section 1.4.1).

Benzenethiol can be applied to a gold surface using either vapor or solution-based techniques. In all experiments performed in this research, a solution-based deposition was performed on account of the volatility and high toxicity of the thiol class of molecules. Solution-based depositions were carried out as follows.

- A dilute (01.-1 mM) ethanolic solution of benzenethiol was prepared by pipetting 99% pure benzenethiol (Acros Organics) into pure ethanol (Fisher Scientific) in a fume hood. The solution was agitated by hand for 60 seconds to ensure good mixing.

- Gold substrates to be functionalized were cleaned by rinsing in ethanol for 60 seconds and then blown dry with N_2.

- Gold substrates were immersed in the prepared benzenethiol solution. The container was immediately sealed and left at room temperature for 12-24 hours.

- After functionalization, excess benzenethiol was removed by rinsing the substrate with ethanol for 60 seconds followed by deionized water for 60 seconds. The substrate was then blown dry with N_2.

Here, it is important to note that the nanoparticles used in the experiments described in this dissertation ranged from 50-200 nm in diameter and the capping agent to be removed was always trisodium citrate ($Na_3C_6H_5O_7$). In case of smaller/larger nanoparticles and/or the presence of a different capping agent, the time and concentration of the thiophenol solution would have to be adjusted accordingly.

2.5 Electrochemical fabrication of nanorods

All Au-Ag-Au heterogeneous nanorods used in the experiments described in this dissertation were grown using a templated nanowire deposition. Briefly, this technique involves the use of a sacrificial anodic aluminum oxide (AAO) template to confine one dimension of the nanorods (the diameter) while the other dimension (the length) is variable and determined by the nanorod growth/electrochemical deposition time [52, 70].

2.5.1 Materials and instrumentation

A commercial potentiostat (PST050, Radiometer Analytical) was used to chemically migrate metal ions into a template with a Pt counter electrode and a Ag/AgCl reference electrode. Au plating solution (Orotemp 24) and Ag plating solution (Silver 1025) were obtained from Technic, Inc. NaOH, ethanol, HNO_3 and high purity aluminum foil were

all obtained from Fisher Scientific. 200 nm anodic alumina oxide (AAO) membranes were obtained from Whatman, Inc.

2.5.2 Method

The preparation of the AAO templates used for the electrochemical deposition of metals begins with the thermal evaporation of a $\sim$ 500 nm-thick Ag layer on one side of the template. This layer has two purposes: (1) to physically seal up the pores to prevent the plating solution from leaking through the templates during electrochemical deposition and, (2) to provide a means of electrical contact between the template and the electrode when it is placed in the electrochemical cell. For the templates used in this research, a special metal holder with holes slightly larger than the templates themselves (13 nm diameter) except for a small segment at the bottom with dimensions 12 nm in diameter was used to suspend the templates in the evaporation chamber. This holder was then suspended at an angle (to ensure that the pores were completely sealed). Ag was then evaporated at a rate of 5-50 nm/s until a thickness of 500 nm was reached. After removal from the evaporation chamber, the templates were used within a few days, as the tarnishing of Ag interferes with the electrodeposition process.

Here it is important to note that the Ag layer on all templates used in these experiments was evaporated onto the "shiny" side of the template. This side is referred to as the "branched" side due to the fact that the pores here do not typically run parallel to one another, but rather diverge like the branches of a tree. By evaporating Ag onto this side, the electrochemical deposition of metals is facilitated as it avoids the necessity of

accounting for branching during the process.

The prepared AAO templates were then placed into an electrochemical cell with the thermally-evaporated layer facing the working electrode. The cell was then assembled and filled with Ag plating solution. The Ag layer deposited here is used as a sacrificial layer because the bottoms of the AAO pores are not parallel and exhibit significant branching. Deposition was performed using the chrono coulometry method in the Voltlab software. The initial deposition was performed at -1 V and was allowed to proceed until -2 C of charge was passed through the cell based on the integration of current versus time (automatically performed by the software). This step is typically completed within 10 minutes, after which the cell is rinsed with distilled water 3 times before depositing the next layer of metal using the same method with the number of coulombs deposited being modified as needed to produce the desired segment length.

Upon completion of the nanowire deposition, the Ag deposited in and on the AAO is removed by submerging the AAO into a diluted solution of nitric acid in order to remove the thermally-evaporated and electrochemically-deposited Ag, and is then rinsed with distilled water to stop the etching process. The nanowires are then released from their template by immersing the AAO in a 0.05 M solution of NaOH and are left overnight until the AAO is completely dissolved, producing free nanowires. Particulate matter resulting from the dissolution of the AAO was removed by washing the nanowires 3 times in ethanol via centrifugation for 20 seconds at 8000 rpm.

2.6 Numerical techniques

One of the main goals of this dissertation is to address the difficulty in reconciling experimental results with theoretical predictions. As such, all of the experimental results presented in the following chapters are compared with numerical simulations based on classical electromagnetic theory. The following is a brief overview of the three distinct numerical techniques used for data analysis.

2.6.1 Mie theory and Generalized Mie theory (GMT)

As described in the overview of the SERS enhancement, the electromagnetic enhancement provides, by far, the greatest contribution to the effect. Furthermore, classical theory provides a quantitative understanding of most characteristics of SERS, including variation with respect to enhancement wavelength, polarization, nanostructure morphology and the type of metal the SERS-active substrate is made from. Unfortunately, realistic estimates of SERS EFs arising from a nanoparticle of arbitrary shape are, in general, not straightforward and invariably require approximations. However, in the case of spherical nanoparticles, the Mie approach utilizes the fact that the field equations can be expressed analytically as infinite sums of vector spherical harmonics [45]. Although these analytical expressions are very complicated, they provide an exact solution for the near fields at the surface of the particle which then be used to solve for quantities such as extinction cross-sections and enhancement factors. Although mathematically complicated, Mie theory is widely accepted as a powerful technique that can be used to model fields in and around nanospheres as well as to check the validity of approximations made

in simulations using other numerical techniques.

Generalized Mie theory (GMT) is the natural extension of Mie theory to an arbitrary number of spheres. Because the largest local field enhancements in nanoparticle aggregates typically arise from gap-plasmon resonances, GMT provides a means of accurately estimating SERS EFs in a more complicated system. Because it is so complex, the application of GMT to problems in SERS has been limited. Nevertheless, it has played an important role in understanding the SERS enhancement that occurs at the interparticle gap between two closely spaced nanospheres (i.e. the nanosphere dimer) [15, 86, 38, 87, 28]. The GMT code used for all calculations described in this dissertation was written by Hongxing Xu of the Chinese Academy of Sciences in Beijing and carried out by students in his research group. A detailed description of this equations and implementation of this code can be found in reference [83].

2.6.2 The Finite-difference Time-domain (FDTD) method

In the FDTD approach, space and time are divided discretely. The volume making up the object of interest is segmented into cubical cells that are smaller than the wavelength of the excitation source. These segments, called "Yee cells", contain the relevant electromagnetic fields (Fig. 2.8). Time is quantized into small steps which, for each segment, represent the time required for the field to travel across a single cell. Because magnetic and electric fields are spatially offset, they are calculated using what is termed a "leapfrog" scheme where the two fields are alternately calculated as the field moves from one Yee cell to the next. In essence, the idea behind FDTD is to create the closest

morphological approximation as possible to the object of interest using boxes, then solve Maxwell's equations inside each box to deduce the fields everywhere. It is this simplicity that defines FDTD's appeal - it is intuitive and simple enough even to be used in a spreadsheet editor such as Microsoft Excel.

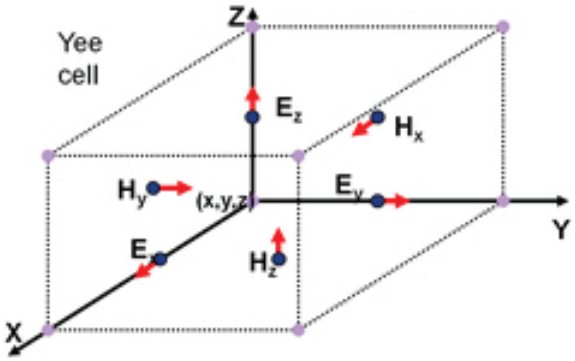

Figure 2.8: The Yee cell with labeled field components.

While the application of FDTD is fairly straightforward in the case of rectangular geometries, modeling the curved surface of spheres requires more careful consideration. Because an array of cubes can only *approximate* a curved surface, it is important that the size of the boxes (i.e. "mesh" size) be small enough to obtain results that converge. However, because the time it takes to run a simulation scales with the cube of the number of cells, one cannot refine a mesh indiscriminately. In case of curved surfaces (as with the dimers studied in this research), factors such as placing mesh override regions in key areas were key to obtaining converging solutions in a timely manner [36, 90, 37]. All FDTD results that appear in this dissertation were carried out using the FDTD Solutions software package (Lumerical Solutions, Inc.)

2.6.3 The Finite Element Method (FEM)

The mathematics of the Finite Element Method (FEM) approach are more complicated than they are for FDTD but, in essence, FEM is used to find *approximate* solutions to partial differential equations and integral equations that describe a specific process. This is done by creating equations that approximate the equations to be studied (in this case, Maxwell's equations) in such a way that is numerically stable (i.e. the results of intermediate calculations don't generate large numbers of errors that would affect the validity of the resulting output) [27].

The meshing techniques for FEM are different from FDTD's in that a "web" of tetrahedrons is used to simulate an object's volume. This approach is much more versatile than the the cubic volume approach and was implemented for experiments involving non-spherical dimers in this dissertation. All FEM simulations were performed using the COMSOL Multiphysics RF module.

Chapter 3

High-throughput Gold Dimer Fabrication Using Capillary Force Deposition

We are at the very beginning of time for the human race. It is not unreasonable that we grapple with problems. But there are tens of thousands of years in the future. Our responsibility is to do what we can, learn what we can, improve the solutions, and pass them on.

-Richard P. Feynman

3.1 Introduction

As discussed in detail in the introductory section, the discovery of SERS provided an avenue around the intrinsic signal strength problems associated with Raman spectroscopy and has prompted a renewed interest in the technique for a broad range of applications, especially in the area of trace-level analyte detection. However, irreproducible EFs arising from the extreme sensitivity of the SERS process to nanocluster morphology, wavelength

and polarization of excitation source, and, perhaps above all, the interparticle spacing and resultant plasmon coupling [26, 20, 31, 72, 13, 11, 18, 85, 19, 62] has severely limited progress towards Raman detection of very dilute analytes. Although theoretical studies have been carried in attempt to understand these effects, here have been few successful attempts to tease out these behaviors from real nanoscopic features since a reliable method for the timely fabrication and systematic testing of these features remains elusive. Advances in electron and ion beam lithography have made it possible to control the morphology and location of particles down to a few nanometers, but such precision is still insufficient to test these effects. On the other hand, other groups have succeeded in linking gold nanoparticles in a controlled manner to create small clusters with known interparticle spacing [68, 5] but the process is low throughput and, more importantly, produces random cluster orientations that obscure the results of the characterization.

In this portion of this dissertation, theoretical predictions regarding the SERS enhancement are addressed experimentally by making measurements of the enhancement factors produced by clusters of a specific size and morphology. Recognizing that the key to characterization of this effect lies in the ability to produce large quantities of nearly identical clusters, this problem was approached using a technique that deftly exploits the advantages of parallel fabrication. Metal nanoparticles were directed to form large, ordered arrays of only dimers with controlled size, orientation, and placement with respect to fiducial patterns. Here, the degree of dependence of the SERS enhancement factor on different parameters was possible. Specifically, a 10^9 enhancement factor was measured for two closely spaced 60-nm gold nanospheres with a marked sensitivity to

the polarization angle with respect to the dimer axis.

3.2 Methodology

3.2.1 Generalized Mie theory simulations

A strong polarization dependence is the clearest indication of an active hot spot. This is rooted in the fact that when metal nanoparticles are brought close together and illuminated with light of the correct wavelength, the resulting plasmon dipole modes can couple via near-field interaction. This coupling gives rise to SERS enhancements which peak in the hot spot when the excitation source is polarized parallel to the dimer axis and, likewise, reach a minimum when the polarization is rotated 90°. To illustrate this, generalized Mie theory simulations [39, 82, 65] were carried out using a program developed by Hongxing Xu [83] for the electromagnetic enhancement in the area immediately around two gold nanoparticles. As mentioned in section 1.3.3, the Raman enhancement can rigorously be shown to be proportional to the product of the squares of the field enhancement factors at the incident and Raman frequencies $G = |f(\omega_{\mathrm{L}})|^2 |f(\omega_{\mathrm{R}})|^2$. Provided that $|\omega_{\mathrm{R}} - \omega_{\mathrm{L}}|$ is smaller than the spectral response of the metal nanostructure, the Raman scattering enhancement scales roughly with the fourth power of the electric field enhancement:

$$G(\mathbf{r}) \approx \frac{|E_{\mathrm{loc}}(\mathbf{r})|^4}{|E_{\mathrm{Inc}}(\mathbf{r})|^4} \tag{3.1}$$

Since the molecular species to be detected could be located anywhere close to the metal surface, the Raman enhancement factor must be averaged over the entire cluster surface:

$$\langle G(\mathbf{r})\rangle = \frac{1}{\sum_{\mathrm{i}}^{2} 4\pi R_{\mathrm{i}}^{2}} \sum_{\mathrm{i}}^{2} \int_{\mathrm{i}} G(\mathbf{r}) d\sigma \tag{3.2}$$

where R is the metal nanoparticle radius and the sum is carried out to two to account for the individual spheres that make up the dimer.

Our simulation comprises two nanospheres 60 nm in diameter separated by an interstitial gap ranging from 0.75 to 4 nm. In the case of parallel polarization, the total Raman enhancement is shown to be strongly dependent on the separation of the particles and the excitation wavelength (Fig. 3.1(a)): enhancements blue shift and decrease at a staggering rate of approximately one order of magnitude per nanometer of separation. Conversely, the total Raman enhancement factor is shown to drop off dramatically as the polarization angle with the dimer axis increases, bottoming out at levels analogous to that of an uncoupled nanoparticle (Fig. 3.1(b)). For the dimer, this polarization sensitivity is a crucial characteristic of the hot spot since this relationship weakens with increasing interparticle gap.

3.2.2 Array fabrication

A combination of chemical and physical methods to control different length scales has enabled us to experimentally confront the simulation predictions. Nanolithography tools are used to make a template to control scales in the 100-nm range, while molecular spacers

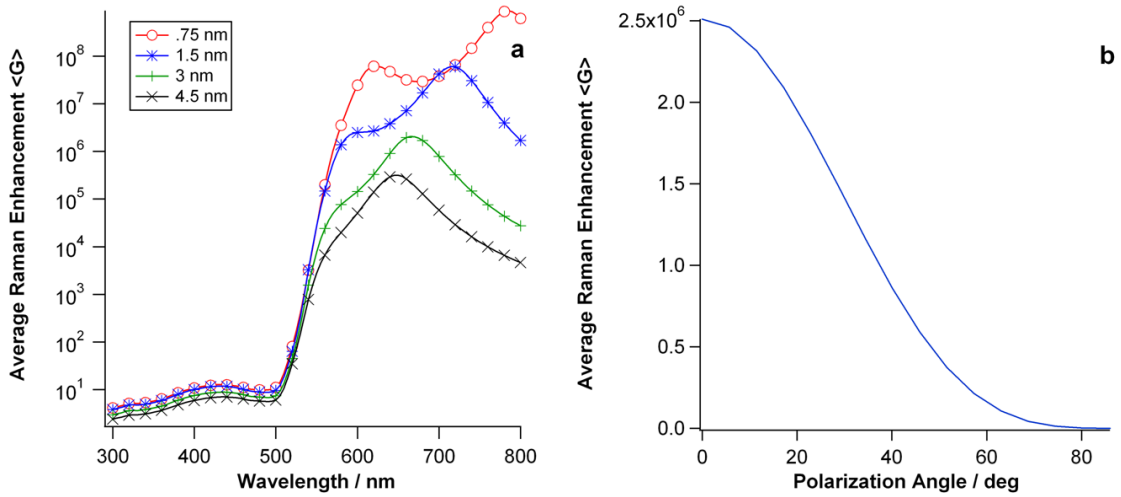

Figure 3.1: (a) Results of GMT simulations of the surface-averaged Raman enhancement over the surface of two 60-nm gold spheres over a range of spacings. Projected Raman enhancement would go roughly as the square of the field intensity. (b) Raman enhancement factor as a function of incident polarization for two 60-nm gold spheres separated by 1.5 nm and illuminated with light of wavelength $\lambda = 632.8$ nm. The refractive index for the surrounding medium in both calculations is set at n = 1.5.

are used to modify and hold the spacing between nanoparticles. The process presented here serves to create localized dimers as well as place them in large-scale arrays.

Template fabrication using PRINT

Large-scale nanoparticle placement is facilitated by the use of a grid of nanoholes in a silicon substrate. This structure is fabricated by applying current advances in low-cost/large-area PRINT technique described in section 3.2. To create the templates used in this experiment, a silicon wafer with a 300 nm-thick film of SiO_2 was used. A 100-nm thick film of poly(lactic-co-glycolic acid) (PLGA) was deposited on the wafer by spincasting a 2 wt % solution of PLGA in acetone at 2000 rpm for 60 sec. A liquid PFPE precursor solution comprising 4.0 kg/mol PFPE α,Ω-functionalized dimethacrylate

and the photoinitiator 2,2-diethoxyacetophenone (0.1 weight %) was poured over a 200 nm by 600 nm cylindrically patterned master template. The liquid precursor was then crosslinked using UV photoirradiation ($\lambda = 365$ nm) for 3 min under a constant nitrogen purge. The fully cured PFPE-DMA elastomeric mold was then released from the master template. A hot plate was set to 90°C and the Si wafer with PLGA film was heated for 1 min before use. The PFPE mold was then thermally laminated to the PLGA-coated Si wafer using a heated laminator set at 19 V for heat and 9.5 V for speed. The lamination step was repeated two more times, without removing the mold from the Si wafer, to ensure efficient pattern transfer. After cooling to room temperature, the PFPE mold was rapidly but steadily peeled away from the Si wafer, leaving a patterned array of PLGA posts on the surface (Fig. 3.2(a)).

The wafer was then placed in a reactive ion etcher and directionally etched for 45 s to remove the flash layer. Next, 20 nm of Cr was deposited on the posts by electron beam evaporation. After the Cr deposition was complete, the sample was sonicated in acetone for 60 min to remove the PLGA posts and expose the SiO_2 originally masked by the polymer, creating an array of circles masked by Cr. The sample was then placed in the reactive ion etcher and etched for 90 s to create 100-nm deep pits in the unmasked SiO_2. Once the dry etch is complete, the Cr mask was removed using CR-14 chrome etch (Transene) and then rinsed in a 2% sulfuric acid solution to remove precipitates from the chrome etchant (Fig. 3.2(b)). Atomic force microscope measurements confirm the final product as an array of 120-nm wide by 100-nm deep holes with a center-to-center spacing of 350 nm (Fig. 3.2(c)).

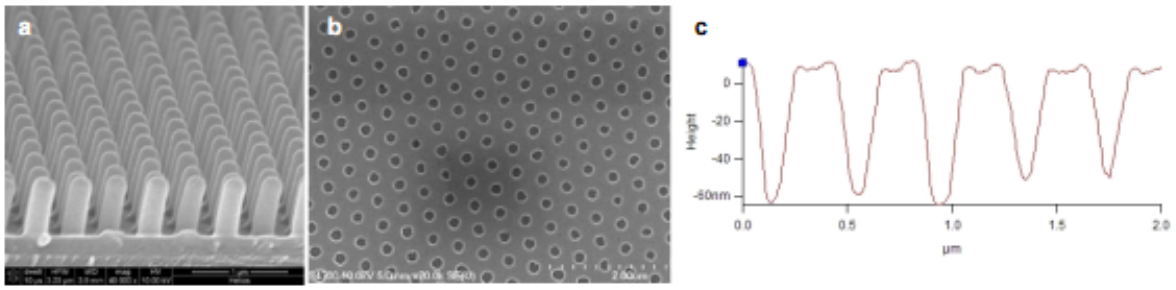

Figure 3.2: SEM micrograph of (a) embossed PLGA posts using a 200 x 600 nm PFPE mold and (b) Cr etch mask after sonication to remove the PLGA posts. (c) AFM data of the final SERS template.

Dimer formation through capillary force deposition

The nanoparticles are positioned in the hole arrays by a capillary force deposition method.[7] To achieve this, a 1 cm^2 piece of nanopatterned substrate is subjected an O_2 plasma treatment for 15 minutes on high to make the SiO_2 surface hydrophilic. The sample is then immediately immersed vertically in a 1 mL sample vial (Eppendorf) filled with an aqueous gold nanoparticle colloid of 60 nm citrate-capped nanospheres (Ted Pella). The solution is left to evaporate in a a vibration-free environment in an oven set to 60°C for 12 hours. As the meniscus slowly recedes across the substrate, nanoparticles concentrate at the three-phase contact line. Because the 120-nm diameter holes can hold only two nanoparticles, several large areas of the substrate contain mostly dimers when the process is complete. Finally, individual dimers were identified on the silicon substrate via electron microscope imaging (Fig. 3.3(a)). Note that the dimers in Fig. 3.3(b) are randomly oriented within the wells (the original master was composed of circular cylinders and was not intended for this application). Dimer orientation cannot be determined optically for this particular sample, making it difficult to verify the accuracy of on- and

off-axis polarization measurements. In order to more precisely position nanoparticle pairs, focused ion beam (FIB) milling was used to fabricate a master template of rectangular wells tailored to the dimensions of the dimers (Fig. 3.3(b)). These wells provide greater spatial constraint for the nanoparticles, which forces the dimers into a definite orientation.

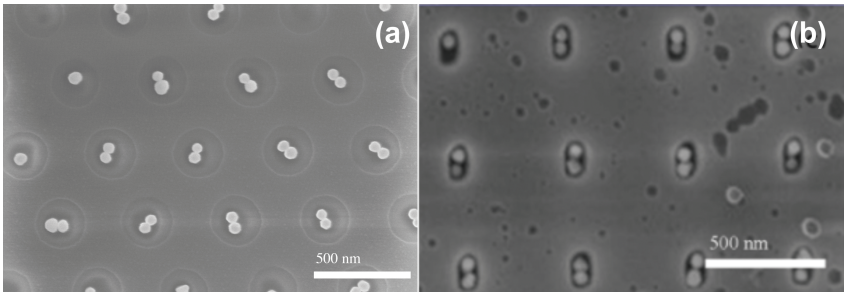

Figure 3.3: (a) gold dimer array fabricated by a combination of pattern replication, wafer processing techniques, and solvent evaporation, (b) gold dimer array fabricated by focused ion beam milling and solvent evaporation.

Benzenethiol functionalization and dimer spacing

When nanoparticles are initially deposited from the gold colloid, they are encased in a monolayer of sodium citrate. In solution, the citrate molecule acts a surfactant, keeping the nanoparticles from aggregating. When they are deposited in the wells, however, the citrate molecules act as spacers, preventing the gold surfaces from touching each other. In order to both control and modify the spacing between nanoparticles, the citrate molecule must be replaced with another rigid molecule. Benzenethiol (C_6H_5SH) was chosen because the high gold affinity of the SH end-groups allows the molecule to easily displace the citrate. Additionally, benezenethiol contains a benzene ring which has a large Raman cross section, making it easy to detect in low concentrations, and its length ($\sim 4.6\mathring{A}$, estimated using ChemDraw) is slightly less than that of a citrate molecule

($\sim 7.2\mathring{A}$), making its placement between two closely spaced nanospheres plausible.

The arrays were immersed in a 0.1 mM ethanolic solution of benzenethiol for 24 h in order to form a monolayer on the gold surface. When the substrate was removed and allowed to dry, the effects of the evaporation pull the nanoparticles together, presumably leaving many dimers with several benezenethiol molecules serving as spacing agents in the interstitial gap.

3.2.3 Microscope setup and SERS measurements

Direct measurement via electron imaging of this spacing was intentionally avoided to prevent potentially deleterious effects on the integrity of the sample. The presence of the bezenethiol molecule in the hot spot was confirmed, however, by subsequent Raman measurements and demonstration of polarization dependence. Raman spectra of individual dimers were taken using a modified confocal microscope outfitted with a flat scanning stage (Nanonics) and connected to a linearly polarized 500:1(632.8 nm) continuous wave (cw) HeNe laser via a polarization preserving, single-mode fiber optic cable. In the microscope, the beam undergoes a collimated path and passes through a high-quality line filter and a $\lambda/2$ wave plate which is used to rotate the beam polarization. The laser is directed to the 150$\times$ microscope objective by a beam-splitting cube which also redirects the collected Raman signal to pass a Raman edge filter prior to being collected by a 100-μm multimode fiber and transmitted to a spectrometer equipped with a low-noise charge-coupled device (CCD) detector (Fig. 3.4). All optics, including the beamsplitting cube, collimators, fiber optics, line and edge filters, and lenses inside the microscope are

nonpolarizing. Power delivered to the sample across all polarizations was confirmed to be uniform within a 3% margin. A diffraction-limited 300-nm laser spot size was verified by imaging calibration grids of feature size above, below, and at the 300-nm limit. Preliminary tests indicated that, without sufficient filtering, persistent exposure to the laser beam caused the benzenethiol monolayer, and consequently the Raman signal, to rapidly degrade. To avoid thermal ablation of the monolayer over the several measurements taken of each dimer to confirm the polarization dependence, the stability of the Raman signal was monitored over a range of beam powers and exposure times. These tests determined that the combination of a 65-μW laser power delivered on the sample with a 5-min acquisition time yielded sufficiently clear and stable spectra.

3.3 Results and discussion

Raman spectra of gold dimers were taken while varying the polarization of the incident beam through a range of 90° relative to the dimer axis. Because the orientation of the dimers was predetermined, measurements through this full range were performed only for a small number of clusters. Most of the dimers were measured within a 10° range around the two dimer axes.

In this study it was found that peaks measured when the incident beam was polarized in the parallel orientation were nearly 2 orders of magnitude taller than those peaks measured when the beam was polarized in the perpendicular orientation in the best cases (Fig. 3.5 (top)). Here, it is important to note that from the large number of dimers

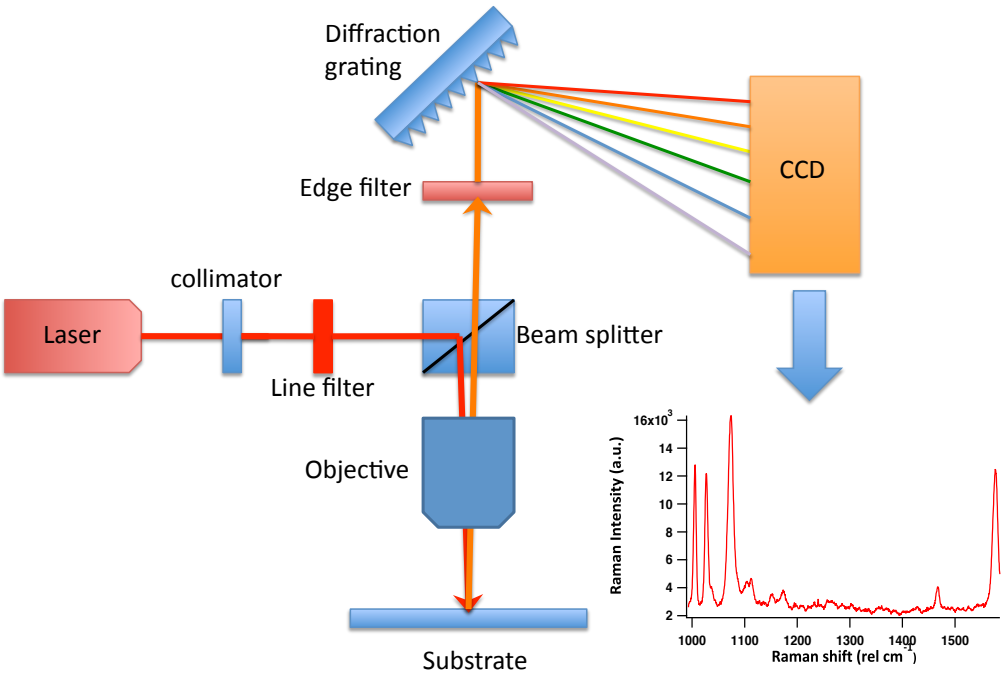

Figure 3.4: Schematic diagram of the Raman microscope setup used in this experiment. The collimator and the line filter are fiberoptically connected, as are the edge filter and the diffraction grating.

measured (50) the mode value of the polarization contrast was approximately a factor of 15 (see inset, Fig. 3.5 (top)). This was attributed to small variations of the dimer alignment in the wells, variations in nanoparticle size and morphology, and possibly the actual size of the interstitial gap, all of which, according to previous studies [26, 20, 31, 72, 13, 11, 18, 62], have strong effects on the enhancement factor. In particular, the possibility that the benzenethiol molecules do not form a perfect monolayer on the gold surface in the vicinity of the hot spot should be noted. If too few or too many molecules assemble in the area, the interparticle spacing can be altered, drastically affecting the size of the enhancement factor. Nevertheless, the polarization contrast supports that hot spots do exist between these nanoparticles.

Additionally, the peak heights in the cross-polarization measurements were within a factor of 2 of the peak heights for isolated nanoparticles. This confirms, along with polarization contrast data, that most of the enhanced Raman signal comes from a small and highly localized area. By calculating the size of this small area and attributing the difference in Raman signal between the two polarization states to the few molecules located there, it was possible for the enhancement factor for the hot spot to be estimated. Specifically, the Raman signal from bulk benzenethiol was measured in a solution of known concentration and compared the per-molecule signal strength with the per-molecule signal strength at the hot spot. The enhanced signal was assumed to arise entirely from an area spanning $\Omega = 2.4 \times 10^{-2}$ steradian spherical cap (a cone with 10° planar projection determined from simulation data) on each of the two nanoparticles. The surface enhancement factor (G) is defined as the ratio of the per-molecule enhancement from

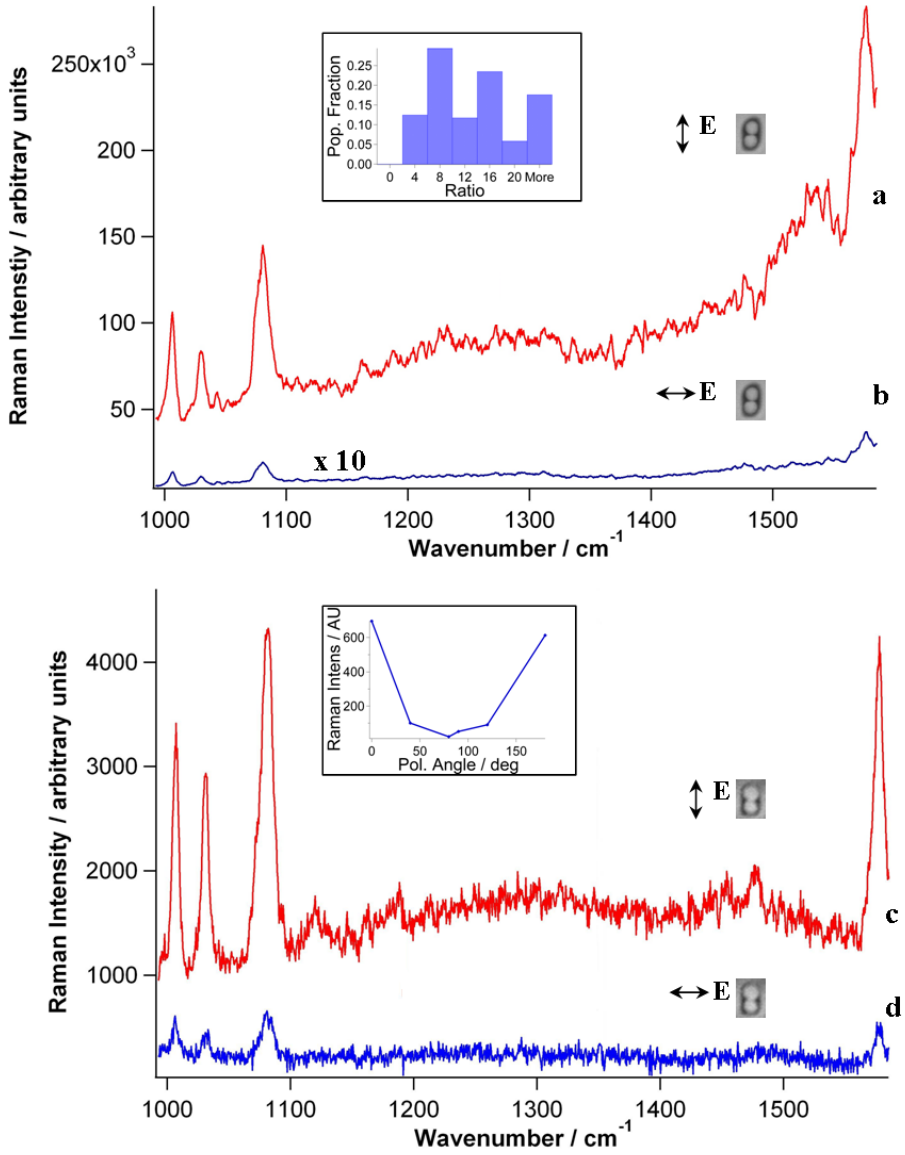

Figure 3.5: Benzenethiol Raman lines measured from a single gold dimer with incident light polarizations (a), (c) parallel and (b), (d) perpendicular to the dimer axis. Traces (a) and (b) in the upper plot are representative of the largest enhancements achieved in this experiment. The inset in this plot is a histogram showing the relative distribution of enhancement ratios between parallel and cross-axial polarization measurements, the largest of which was 79. Traces (c) and (d) in the lower plot are examples of what was typically measured in the polarization studies. The inset shows how the Raman intensity of an individual dimer varies as a function of polarization.

this spherical cap to the per-molecule enhancement from bulk benzenethiol. Thus:

$$G = \frac{I_{\mathrm{SERS}}/N_{\mathrm{Surf}}}{I_{\mathrm{RS}}/N_{\mathrm{Vol}}} \tag{3.3}$$

where N_{Surf} is equal to the number of molecules occupying the area subtended by Ω multiplied by the molecule surface packing density and N_{A} (Avogadro's number). In this calculation, a value of 1.1 nmol cm^{-2} was used, the largest packing density currently reported in the literature [76]. N_{Vol} is defined as follows:

$$N_{\mathrm{Vol}} = \pi r^2 h c N_{\mathrm{A}} \tag{3.4}$$

where r is the radius of the laser spot (150 nm), c is the molar concentration of pure benzenethiol (9.77×10^{-3} mol cm$^{?3}$), and h is the effective focal depth of the objective ($1\ \mu$ determined by moving the objective above and below the focal point until the Raman signal disappears). Using this formula, the number of benzenethiol molecules in the probe volume was estimated to be $N_{\mathrm{Bulk}} = 4.16 \times 10^8$.

The ratio of $I_{\mathrm{SERS}}/I_{\mathrm{RS}}$ was taken on the 1575 cm^{-1} band. After removing the counts from the cross-polarization measurement to approximately separate the central hot spot Raman signal, the ratio was 1397 in the best sample and ≈200 in more typical cases. Both of these values were used to calculate SERS enhancement factors. Ultimately, a range in value of 10^8-10^9 was arrived at for the enhancement factor relative to the signal from bulk benzenethiol. For cross-polarization measurements, the enhancement factor resulted in 10^3 - 10^4 and was calculated in the same way but under the assumption that all the

benzenethiol molecules coating the dimer surface contribute in equal proportion to the Raman signal. These measurements compare well with those of single gold nanoparticles [26, 20, 31, 72, 13, 11, 18, 62], and confirm that the multiparticle enhancement is not simply the sum of individual particle contributions.

Finally, it should be noted that this technique lends an enormous amount of versatility to this study. Gold nanoparticles can be removed from substrates by treatment with aqua regia (a 1:4 mixture of HCl and HNO_3), so a single sample can be reused repeatedly. Moreover, while benzenethiol was used in this experiment, molecular linkers of different sizes would add a greater degree of certainty to the gap size and could be used to achieve a wide range of interparticle spacings. Finally, features of virtually any size and shape down to 80 nm can be patterned into these substrates, allowing the fabrication of more complex clusters and arrays. Simulations performed in a recent study indicate that chains of several nanospheres can produce enhancement factors greater than those observed from dimers [74]. In the following chapter, the experimental testing of this theory utilizing the capillary force deposition technique to create nanochains of nomimal length is described.

Chapter 4

Investigation of the Relationship Between Nanoparticle Chain Length and SERS Enhancement Factor Strength

It doesn't matter how beautiful your theory is, it doesn't matter how smart you are. If it doesn't agree with experiment, it's wrong

-Richard P. Feynman

4.1 Introduction

In section 1.5, the topic of aggregates of metallic nanoparticles being used as efficient and effective SERS-active materials with the spherical nanoparticle dimers being among the most simple (and consequently, one of the most popular) choice of configuration. In a recent study, the question has been posed as to whether a two-particle linear aggregate is, indeed, the optimal configuration for generating SERS enhancements, prompting researchers to consider other morphologies [74]. One such configuration is closely spaced

metal nanoparticles (a natural extension of the dimer configuration) arranged end to end to form a chain. This structure was theoretically investigated by Wang *et al.* [74], who carried out finite integral technique (FIT) simulations on gold and silver nanoparticle chains comprised of even numbers of nanoparticles ranging in length from 2 nanoparticles to infinity. The results of these simulations indicate that the field enhancement at gap between the two centermost particles (Wang refers to this as the "c-point")can reach a maximum at a number larger than two, suggesting that the dimer might not always be the ideal configuration for achieving maximum field enhancement. In contrast to these predictions, however, recent theoretical and experimental results by Wustholz *et al.* [78] suggest that, in most realistic experiments, the signal from the hottest hot spot in a cluster is often extremely dominant and, thus, renders irrelevant any possible enhancement due to near-field coupling along the chain as a whole. In this report, the main aim is to test these conclusions on precisely designed nanoparticle chains. Through the combination of capillary force deposition [7] and template fabrication via FIB milling, closely spaced linear nanoclusters were fabricated. The SERS enhancement arising from these structures were measured and subsequently compared with theoretically predicted values.

4.2 Numerical simulations

4.2.1 Generalized Mie theory simulations

Because it was not possible for us to measure the SERS EF directly at the c-point, we have carried out generalized Mie theory (GMT) [45, 82, 84, 39] simulations to map the electromagnetic field strength over the entire surface of gold nanosphere chains ranging in length from 1 to 9 nanoparticles with interparticle separations of 1 and 1.5 nm (these separations still yield reliable results in the frame of classical electromagnetic theory). Fields were calculated at a distance of 0.5 nm from the metal surface which, based on the estimated thickness of the benzenethiol monolayer (the reporter molecule used in the experimental part of this study), is the most likely location of the reporter molecule. The Raman enhancement is proportional to the product of the squares of the field enhancement factors at the incident and Raman frequencies. Here, it is important to clarify that this method was designed to produce results that could be compared with experimental measurements of the SERS EF in an attempt to see if larger enhancements *could* be obtained experimentally and/or theoretically using the surface averaged approach. As a result, our computational approach does not directly mirror the FIT calculations performed by Wang *et al.* and is not intended to prove or disprove the validity of those results.

As with the calculations performed in section 4.2.1 the $|E|^4$ (i.e. zero-Stokes shift) approximation is used and the Raman enhancement factor is averaged over the entire chain surface at a distance of 0.5 nm from the surface of the metal (where the molecule

of interest is most likely to be located). Although the length of the molecule and bond length for benzenethiol adsorbed on gold are well known, the interparticle distance for the structures fabricated in this experiment cannot be known exactly. Similarly, the index of refraction of liquid benzenethiol is different from that of monolayer surrounding the nanospheres. To account for this range in gap size and the effective refractive index of the surrounding medium, n_{eff} , the surface-averaged enhancement was calculated for a gap of 1 nm and $n_{\text{eff}} = 1.0$ (Fig.4.1(a)) as well as for a gap of 1.5 nm and $n_{\text{eff}} = 1.5$ (Fig. 4.1(b)). Significantly, a peak is apparent in the Raman enhancement at a chain length of 3 nanoparticles for the 1 nm gap ($n_{\text{eff}} = 1.0$) and 2 nanoparticles for the 1.5 nm gap ($n_{\text{eff}} = 1.5$). It is well known that the aggregation of nanoparticles causes the plasmon resonance frequency to shift to longer wavelengths. Thus, it is presumed that these enhancement peaks correspond to the resonance peak crossing the laser line.

4.2.2 Finite Difference Time Domain (FDTD) simulations

To exemplify the link between nanoparticle chain length and the location of the Raman enhancement peak, the extinction spectra for linear chains was calculated using the finite distance time domain (FDTD) method (Lumerical Solutions, Inc). Results from these simulations are shown in Fig. 4.2. First, the redshift of the extinction peak with respect to the increased particle number is apparent, indicating as expected, the tight correlation between the optical response and the morphology of the scatterer. Most importantly, however, location of the highest peak of the extinction along the x-axis coincides with the location of the SERS EF peak in Fig 4.1. This provides a strong

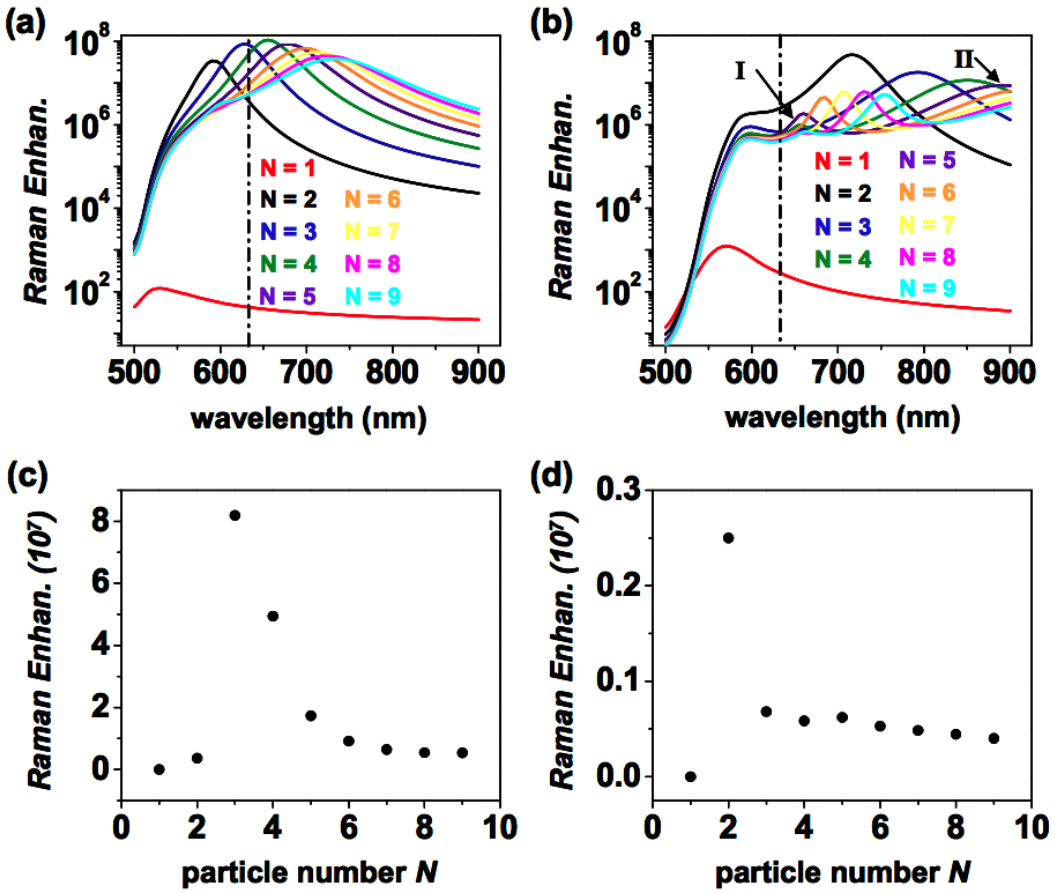

Figure 4.1: Calculated SERS EFs for Au nanoparticle chains using generalized Mie theory. The EF spectra have been calculated for chains ranging 1-9 nanoparticles in length with excitation source parallel to the long axis of the chain for an interparticle gap of 1 nm and $n_{\text{eff}} = 1.0$ (a) and an interparticle gap of 1.5 nm and $n_{\text{eff}} = 1.5$ (b). The EF for the 632.8 nm excitation source for (a) and (b) are shown respectively in (c) and (d). Angular momentum contributions up to the 37th order were included in the GMT calculations. The integral was taken at a distance of 0.5 nm from the particle surface for (a) and 0.75 nm from the particle surface for (b). The two enhancement peaks for the N=5 chain are identified as II and I, respectively, in (b).

indication that the localized surface plasmon resonance (LSPR) peak of the structure (defined by the geometry of the chain as well as the physical properties of the metal the nanostructure is composed of) is in resonance with the laser. Thus, in this particular case involving 60 nm gold nanoparticles, it can be assumed that the ideal chain length producing the largest SERS response can, indeed, be longer than a dimer under certain conditions.

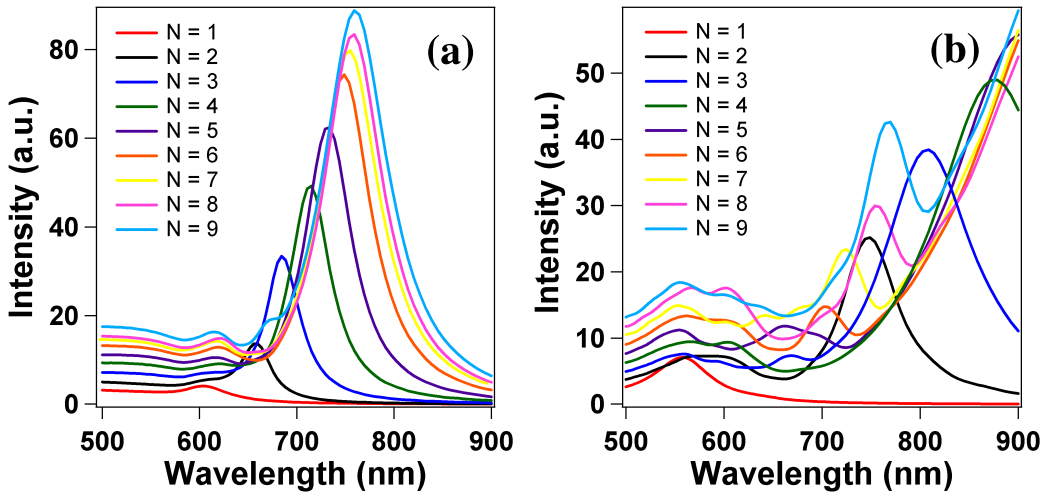

Figure 4.2: FDTD calculations of the extinction spectra for 60 nm Au nanoparticle chains 1-9 nanoparticles in length. Nanochains in (a) have a 1 nm interparticle separation and are embedded in a medium with refractive index $n_{\text{eff}} = 1$. Nanochains in (b) have a 1.5 nm interparticle separation and are embedded in a medium with refractive index $n_{\text{eff}} = 1.5$

4.2.3 Substrate fabrication

To experimentally test the simulation results, a templating method was employed to create nanoparticle chains of specific lengths and orientations. FIB milling was used to create trenches in SiO_2 which were approximately 80 nm in width, 70 nm in depth and ranging from 80 to 560 nm in length. Gold nanospheres (Ted Pella) with a diameter of

60 nm were placed into these trenches using the same capillary force deposition method employed in section 3.2.2 (Fig. 4.3).

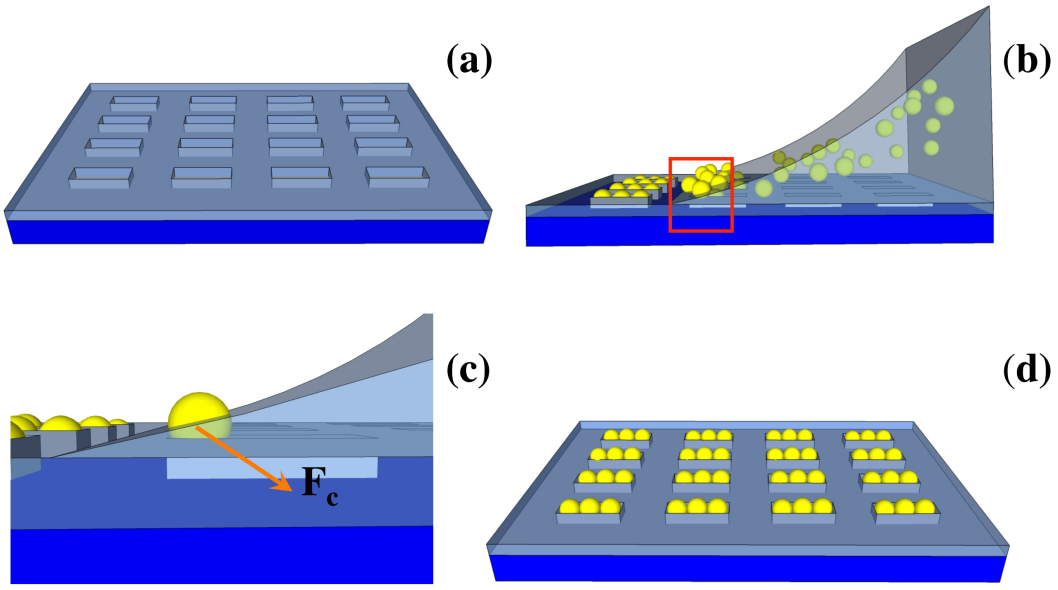

Figure 4.3: (a) Silicon substrate immediately after FIB milling of SiO_2 layer. (b) Illustration of three-phase contact line dragging nanoparticles across the substrate surface. (c) Close-up illustration of particles pushed into milled trenches via the capillary force. (d) Array of nanosphere trimers after deposition is complete.

As mentioned previously, because the trenches are designed to host only a specific number and configuration of particles, this process creates arrays of nanoparticle chains of predetermined lengths. Scanning electron micrographs of the substrates were then taken (Fig. 4.4) to identify satisfactory chains. To remove the carbonaceous contamination that often accompanies SEM imaging, substrates were subsequently cleaned with piranha solution and treated with O_2 plasma for 10 minutes to remove any unwanted material that the electron beam might have deposited (preliminary tests where a follow-up image was taken demonstrated that the cleaning process did not dislodge or drastically move

any of the particles in the chain). Finally, nanochains were functionalized with a SERS-active reporter molecule, benzenethiol. The substrates were immersed in 10 mM ethanolic solution of benzenethiol overnight, removed, rinsed for 60 seconds in ethanol to remove excess benzenethiol, and then blown dry with N_2.

4.2.4 Raman measurements

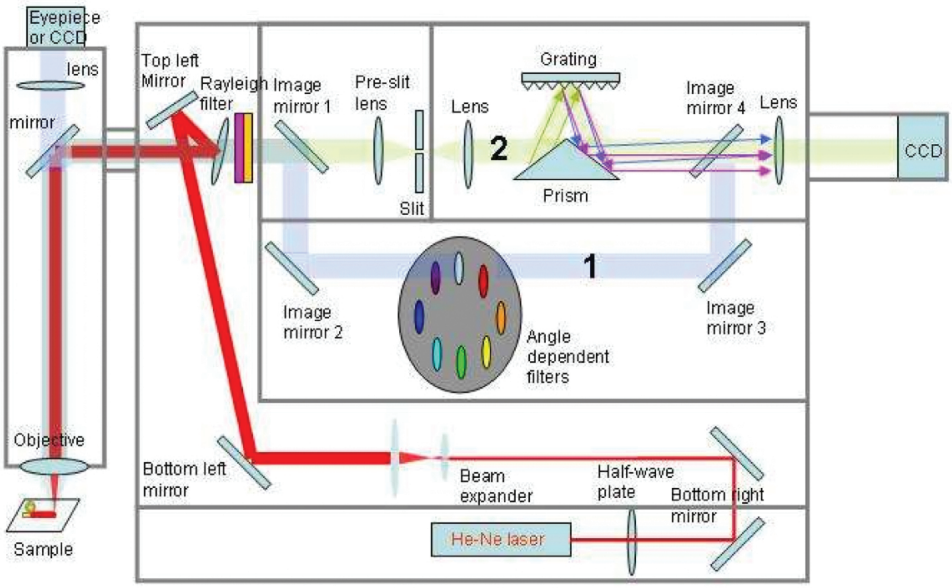

Figure 4.4: Schematic diagram of the Renishaw Invia microscope used in this experiment.[10]

Raman spectra of individual chains were obtained using a Leica microscope equipped with a confocal Raman spectroscopic system (Renishaw InVia) and a 30 mW 632.8 nm laser excitation source (Fig 4.4). All spectra were measured using a 50× objective with a numerical aperture of 0.75. The Raman signal was collected by a TE air-cooled 576 × 400 CCD array preceded by two notch filters (OD > 12) to block the laser line. Preliminary tests concluded that, without sufficient filtering, persistent exposure to the laser beam

causes the benzenethiol monolayer to degrade. To avoid photodegradation of the monolayer, the stability of the Raman signal was monitored over a range of beam powers and exposure times. These tests determined that the combination of a 100 μW laser beam power (spot size diameter $\sim$2 μm) delivered on the sample with a 30 second acquisition time yielded sufficiently clear and stable spectra. To account for the possibility that the laser spot was not perfectly aligned over the chain and/or not perfectly uniform, a flat scanning stage was used to raster over the structure. From these several measurements, the strongest, most well-defined spectrum from each of the structures was selected for data analysis. A typical spectrum for a nanoparticle heptamer is shown in Fig. 4.5. The most pronounced peaks appear at 1000 cm^{-1} (ring out-of-plane deformation and C-H out-of-plane bending),1080 cm^{-1} (C-C symmetric stretching and C-S stretching), and 1577 cm^{-1} (C-C symmetric stretching) [21]. Time-stability tests were performed in order to select the most stable Raman peak for comparison in these tests. All the peaks were clear and steady, but the 1080 cm^{-1} peak was found to show the best signal to noise ratio and was, thus, used for all data analyses performed in this dissertation.

4.3 Results and discussion

Experimental results are plotted over GMT results for a 1.5 nm interparticle gap in Fig. 4.6. Results from two data sets are shown to delineate the range of outcomes for this particular experiment. Specifically, the largest measured enhancements for each chain length (red trace) are provided to represent the most ideal results obtained in this

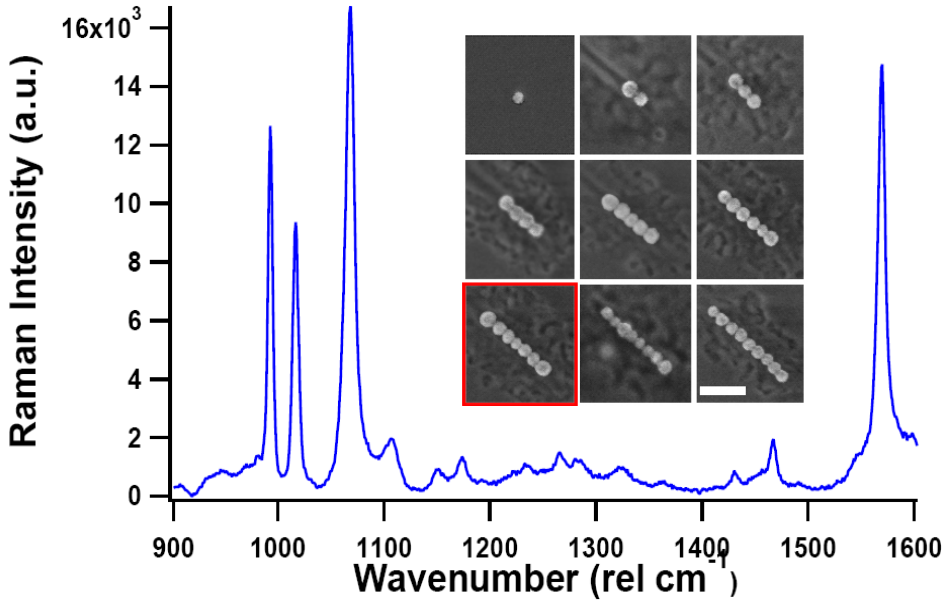

Figure 4.5: (a) Scanning electron micrograph of gold nanochains ranging 1-9 particles in length. Scale bar is 200 nm. (b) SERS spectrum of benzenethiol on a nanochain comprised of 60 nm gold nanospheres. Measurements were taken with a 632.8 nm laser source polarized parallel to the nanochain axis. The red box in (a) denotes the heptamer from which this measurement was taken.

study while a set of results falling within one standard deviation of the data set average (blue trace) is provided to represent results most typically obtained in this experiment (taken from a pool of 30 sample areas for each chain length). While both the ideal and typical results demonstrate the significant increase in the enhancement of the dimer over the monomer predicted by the GMT simulations, the typical results (blue trace) deviate from theory at longer chain lengths, reaching a plateau of enhancement rather than decreasing for larger particle numbers. The large enhancement ratio between the monomer and the dimer is unsurprising, as it is well known the tiny gaps formed by closely spaced nanoparticles are the source of large electric fields which give rise to large SERS enhancement factors. This situation becomes more complex, however, when the number of gaps in the chain is increased through the addition of nanoparticles. It has been shown that the SERS EF is extremely sensitive to interparticle separation, falling off at the rate of approximately one order of magnitude per nanometer of separation[1]. For longer nanochains, a mixture of coupled and decoupled neighboring particles might coexist. Moreover, the extreme sensitivity of the SERS enhancement to a gamut of factors, including nanoparticle size [35], shape [20], crystal face [30], surface roughness [40], and particle-particle spacing [72, 26, 18, 24, 64] is well documented and is known to account for significant variations in EFs arising from seemingly-identical nanoparticle clusters. Taking these two items into consideration, it is unlikely that the enhancement that would arise from a perfectly coupled nanochain of a specific length is being observed. Moreover, it is quite likely that a single dominant hot spot is accounting for the majority of the enhancement observed for all chain lengths > 1. Significantly, these results explain

the plateau of the EF in Fig. 4.6 as well as emphasize the importance of making hot spots through gap formation over additional enhancements achieved through resonances in complex geometries, thereby supporting the Wustholz *et al.* [78] conclusion.

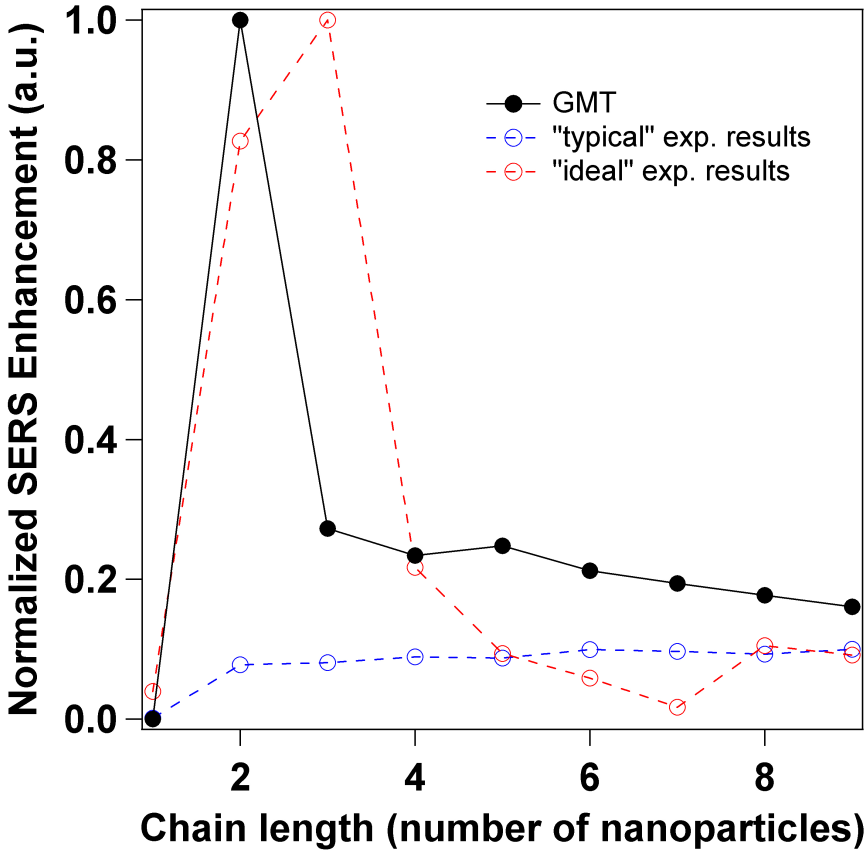

Figure 4.6: Black trace: Generalized Mie theory calculations for the SERS EF for 60 nm diameter Au nanochains with a 1.5 nm interparticle separation, embedded in a medium with refractive index $n_{\text{eff}} = 1.5$. Blue trace: Experimental SERS EF measurements for 60 nm diameter Au nanochains lying within one standard deviation from the average measured EF value for each chain length (i.e. "typical" results). Red trace: Largest values for the SERS EF for each chain length measured in this experiment (i.e "ideal" results). "Typical" results (blue trace) are normalized against the values for the "ideal" results (red trace) to illustrate the difference in magnitude between the two experimental data sets.

At the other end of the spectrum, the ideal results do show a qualitative agreement with theory. While it would be impossible to accurately determine whether the peak

at a chain length of 3 nanoparticles arises from perfect interparticle coupling along the entire length of the chain, it is certainly relevant to include a discussion of this ideal situation. Referring back to Fig. 4.1, despite a small redshift, the maximum Raman enhancement for the monomers depicted in 4.1(a) and 4.1(b) are located around 525 nm and 570 nm, respectively, corresponding to the far-field LSPR peak. For aggregates consisting of more than two spheres, the hybridized plasmon modes appear as a result of the interaction of primary plasmons in nearby spheres [53, 59]. Obviously, this coupling dramatically enhances the local electric field, creating a SERS enhancement that is an order of magnitude larger than that of a single sphere. In addition to lowering the bonding mode, hybridized plasmon modes of higher angular momentum are also excited by the wave polarized parallel to the long axis of the chain. As the chain length is increased, both EF peaks experience a redshift. Surface charge distributions at the EF peaks (660 nm and 890 nm) of the five sphere chain are shown in Fig 4.7. These chains demonstrate a sufficiently strong dipole moment and are, thus, able to couple to far field radiation efficiently, thereby creating the peaks in the EF most certainly observed in both the simulation and experimental data [3].

In summary, GMT and FDTD simulations were performed to model the *surface-averaged* electromagnetic field enhancements arising from plasmonic coupling in closely spaced noble metal nanoparticle chains. The simulations suggest that there exists an "ideal" chain length capable of producing modest improvements on the typical dimer enhancement factor. To experimentally test the model, chains of 60 nm gold nanospheres were fabricated using a capillary force deposition technique. Subsequent Raman measure-

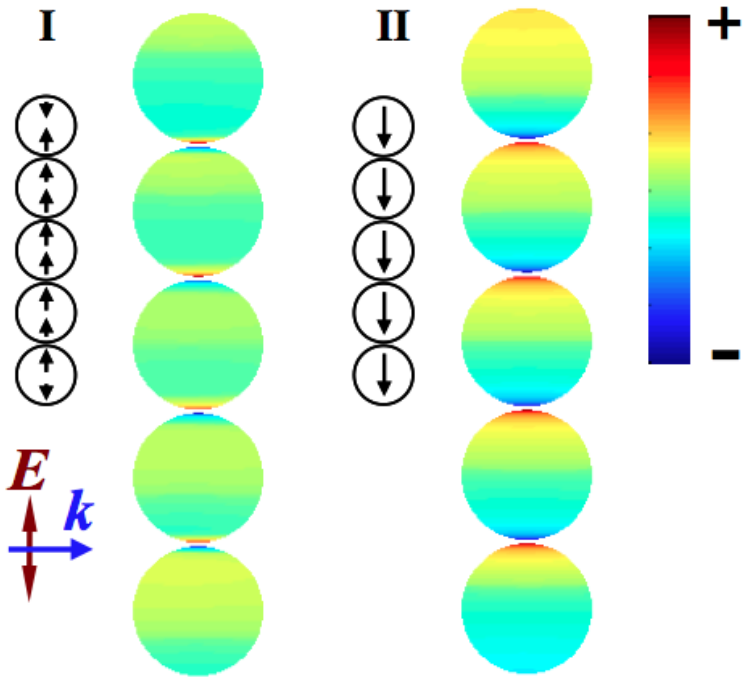

Figure 4.7: Charge plot for identical Au NPs (60 nm in diameter). Gap distances were 1.5 nm and the refractive index of the embedding medium was $n_{\text{eff}} = 1.5$. The highest order of angular momentum included was 37 in the GMT calculations. The bonding and higher-order modes are identified as II and I, respectively.

ments made from these structures showed modest agreement with the GMT simulations in some cases and complete lack of agreement in others. From these results, it was concluded that it is unlikely that the individual nanoparticles comprising the chains made using the capillary force deposition technique are consistently able to couple completely along the entire structure, thereby departing from the ideal situation modeled in the calculations performed in this study. However, comparison of experimental and theoretical results also show that the formation of dimers provides a large improvement in signal strength over the monomer enhancement. While perfect plasmonic coupling of the ideal number of nanoparticles can provide improvement over the dimer enhancement, it is marginal under the best of circumstances and often introduces more difficulties in the fabrication process than is justifiable by the small boost in signal.

Chapter 5

Tunable SERS in Gold Nanorod Dimers Through Strain Control on an Elastomeric Substrate

Any intelligent fool can make things bigger and more complex... It takes a touch of genius - and a lot of courage to move in the opposite direction.

-Albert Einstein

5.1 Introduction

As mentioned previously, theoretical and experimental studies have shown that small variations in a multitude of parameters have a profound impact on particle-particle plasmonic coupling in nanoparticle dimers and the resulting strength of the SERS enhancement. Although this has been a figurative 'thorn in the side' for those who wish to make large-areas SERS-active substrates, it also presents the possibility of creating structures that are infinitely tunable, provided the techniques for fabricating the desired structures.

We have already stated that theoretical studies have shown that variations in particle-

particle spacing have a particularly strong effect on the strength of the"gap plasmons" between highly resonant (<100 nm) particles, with changes in the spacing as small as 1 nm causing the SERS signal to rise or fall by amounts as large as an order of magnitude. For larger particles this effect is less dramatic [57] but nevertheless, the distance dependence of the SERS enhancement has been limited by experimental variation of multiple parameters. In past experiments, researchers have examined collections of seemingly-identical particle pairs with nominally-controlled spacings [72, 18, 64, 48, 61], but which surely possess large variations in the crucial parameters listed above. Even Raman-active molecule coverage cannot be warranted to be identical, thus geometrically similar clusters often present very different SERS effects. While there has been some success producing reliable surface-averaged enhancement factors over large areas [16, 41] the ability to probe specific parametric dependences of the SERS effect itself is inextricably dependent on the ability to make repeated measurements on truly identical individual nanostructures. Therefore, a technique that provides the ability to vary a single parameter (e.g., particle-particle spacing) while holding all the other morphological aspects constant is both desirable and necessary.

In this experiment, a simple method by which the spacing between two adjacent nanorods can be changed by varying the strain applied to an elastomeric silicone rubber substrate is described. The deposition of nanorod dimers on a stretchable substrate permits the coupling of macroscopic changes in substrate length to nanometer-sized movements between particles, resulting in a tunable interparticle gap size. Applying this technique, the interparticle distance dependence of the SERS enhancement of individual

pairs of gold nanorods is verified, the first time that such a feat has been realized. This technique provides several significant benefits: (a) the controlled strain provides access to small interparticle spacings that would otherwise be impossible to achieve with current lithographic methods, (b) particle separation can be optimized, thereby creating maximum SERS signal strength, and (c) the process is completely reversible and repeatable for a given set of dimers. Additionally, this technique relies on basic wet chemical processing techniques and can be easily adapted to a wide range of particle sizes, shapes, and compositions, providing a promising alternative for studies involving the precise placement of nanoparticle structures.

5.2 Methodology

5.2.1 Finite element method (FEM) simulations

Recently, there has been a great deal of interest in extending spectroscopic capabilities to nanogap structures with larger segment lengths. Larger structures provide the option of being addressed electrically and can more easily be identified and tracked using optical microscopy, an important factor in the approach adopted in this study. In contrast to their smaller counterparts, nanostructures several hundred nanometers in length support multipolar resonances [75] that are periodic in nature, providing large enhancements at specific lengths and producing almost no signal at others for a given excitation source frequency [61, 60]. For these experiments, nanorod segments 1 μm in length were chosen, which were expected to present resonant behavior when illuminated with a 785 nm source

according to the relation [40]:

$$L = \frac{n - \frac{1}{2}}{2}\lambda \tag{5.1}$$

where L, λ, and n are the segment length, the surface plasmon polariton wavelength, and the order of the multipole, respectively.

In order to determine the gap dependence of the enhancement factor at the interparticle junction, full-wave electromagnetic calculations based on the finite element method (FEM, COMSOL Multiphysics) were performed. The rod dimer configuration simulated in this study consisted of two cylindrical segments ranging from 200 to 320 nm in diameter and 1 μm in length, consistent with the size of the nanorods produced in this experiment. Incident plane wave radiation impinged normally on the dimer, with the electric field polarized parallel to the dimer axis. Optical constants of gold $(\epsilon_{\mathrm{Au}}) = -23.02 + 1.436i$ at the vacuum wavelength of 785 nm were taken from Johnson and Christy [29]. In order to compare the simulation results with the SERS enhancement factor (EF) obtained experimentally from an adsorbed monolayer, the surface-averaged SERS EF was estimated using the relation [54]

$$G = \frac{\int g\, dS}{\int dS} \tag{5.2}$$

where $g = \frac{|E_{\mathrm{R}}|^2|E_{\mathrm{L}}|^2}{|E_{\mathrm{Inc}}|^4}$ denotes the localized SERS EF and E_{Inc}, E_{R} and E_{L} are the incident, enhanced Raman and enhanced incident electric fields, respectively and the integral was taken over a cross-section in the gap region 1 nm away from the metal

surface. Because the absorption peaks for these rods are broad and the wavelengths of the enhanced excitation and Raman radiation are close enough to fall under the umbrella of this peak, the approximation $|E_{\mathrm{L}}|^2|E_{\mathrm{R}}|^2 \approx |E_{\mathrm{L}}|^4$ was used. The SERS enhancement factor (EF) was evaluated at a distance of 1 nm from the metal surface to avoid breakdown of the classical approach and numerical instabilities at the particle surface as well as to coincide with the distance at which an adsorbed reporter molecule (benzenethiol was used in this study) would likely be located.

The calculated relations between the SERS EF and particle-particle spacing for gold rod pairs 200-320 nm in diameter are shown in Fig. 5.1(a). The results of these simulations reveal optimal gap sizes for these particular rod pairs below approximately 20 nm, indicating the target range for the experimental particle-particle separation studies. Within this range, the dimer is expected to create a surface averaged SERS EF on the order of $\sim 10^5$ when excited at its resonance frequency. Here it is important to note that multiple maxima appear at these small interparticle distances, arising from the plasmon resonances of the gold dimer. As the diameter of the nanorod segment increases, these resonances tend to shift to larger gap separations. Large local electric fields are generated by the electric field enhancements in the gap, which will serve to enhance the Raman excitation of the reporter molecule. The distributions of the E_{x} component of the local electric field for different resonance peaks are shown in Fig. 5.1(b), each corresponding to one peak in the EF-distance relation shown in Fig. 5.1(a). The rod diameters in (i-iii) are 320 nm and 200 nm in (vi). The gap distances are 5 nm, 9 nm, 15 nm, and 20 nm in (i-vi), respectively. It should be noted that in order to evaluate these resonances for

SERS enhancement, the integral over the absorbing surface is critical due to the spatial distribution of the enhanced electric fields. This differs from calculations involving small nanoparticle dimers where the EF from a single position (e.g. the center of the gap) gives a result similar to the surface averaged enhancement factor.

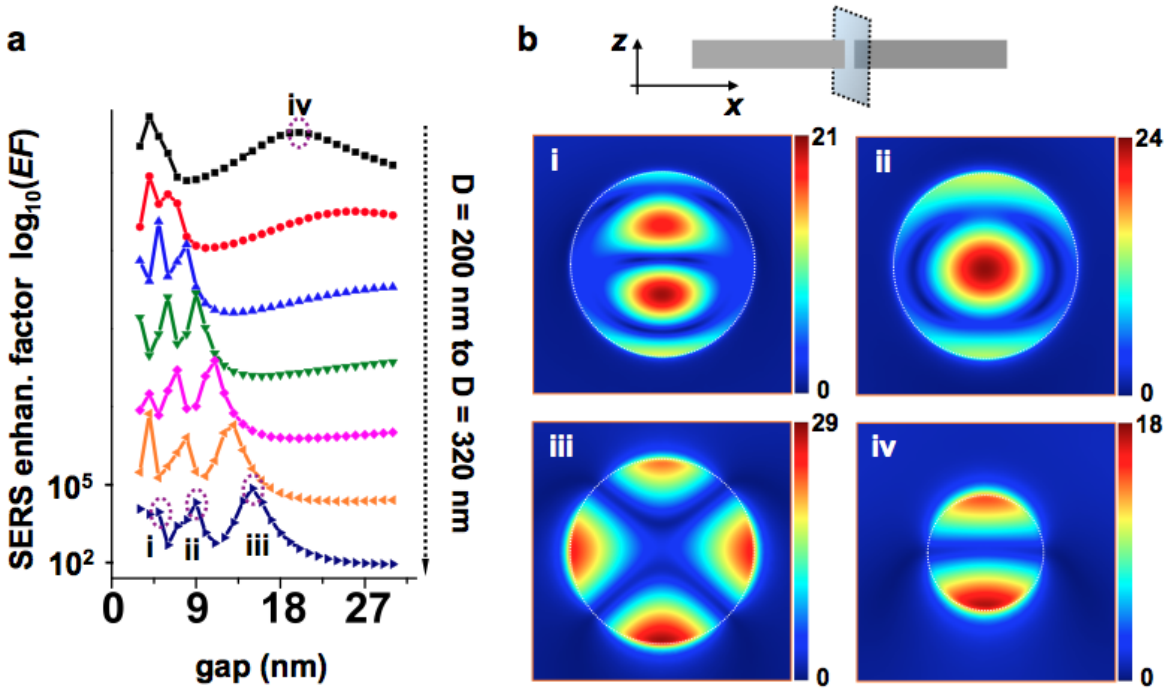

Figure 5.1: (a) FEM calculated surface-averaged SERS enhancement factor (EF) as a function of gap distance for gold rod dimers of different sizes (D = 200 nm to D = 320 nm from top to bottom in increments of 20 nm). (b) Calculated $|E_x|$ distribution in the vertical plane at the center of the gap (indicated in the inset) for modes i to iv

5.2.2 Electrochemical fabrication of gold gapped nanorods

To experimentally realize the dimer configuration described above, nanorod dimers were fabricated using a modified version of on-wire lithography (OWL) [56]. Nanorod dimers were created using a combination of electrodeposition and wet chemical etching.

Au-Ag-Au nanorods were grown via DC electrochemical deposition in 200 nm-diameter anodic alumina oxide (AAO) templates (Whatman). For this experiment, two Au cylinders (1 μm in length) were separated by a Ag segment (~ 80 nm in length) designed to serve as a sacrificial spacer layer. Immediately following the electroplating, the templates were placed in a 3 M NaOH solution for 60 minutes to dissolve the alumina and, afterwards, were washed in ethanol and suspended in a 20:80 mixture of ethanol and water to prevent aggregation. A typical nanorod dimer pair is shown in the inset of Fig. 5.5. SEM imaging provided information about the dimensions of the nanorods constituting a typical dimer pair. The diameters of the resulting nanorods are defined by the pores in the host AAO template (nominal values ranging from 200-320 nm). Nanorods were then dropcast on a pre-strained silicone rubber film and blown dry with N_2 (Fig. 5.2a). The use of heterogeneous nanorods as a precursor structure provides several technical advantages over randomly-deposited nanostructures previously used in SERS experiments [48, 51, 21]. One of the most significant advantages is customizable gap sizes designed into the resulting nanorod dimer pair after etching of the sacrificial layer. Other researchers used an oxide backbone to fix the particle interspacing [61]. However, in the approach used here this distance is not critical and in fact it just needs to be in the desired range since it will be tuned via the elastomeric substrate. Next, the film was immersed in a 6 M aqueous solution of HCl and water for 10 minutes at room temperature to etch away the Ag spacer (Fig. 5.2b). The substrate was then removed from the HCl solution and rinsed in deionized water for two minutes to remove excess HCl. Finally, the completed dimers were immersed in a 1 mM ethanolic solution of benzenethiol (BT) for 24 hours at

room temperature to ensure thorough functionalization of the nanorods with the reporter molecule (Fig. 5.2c).

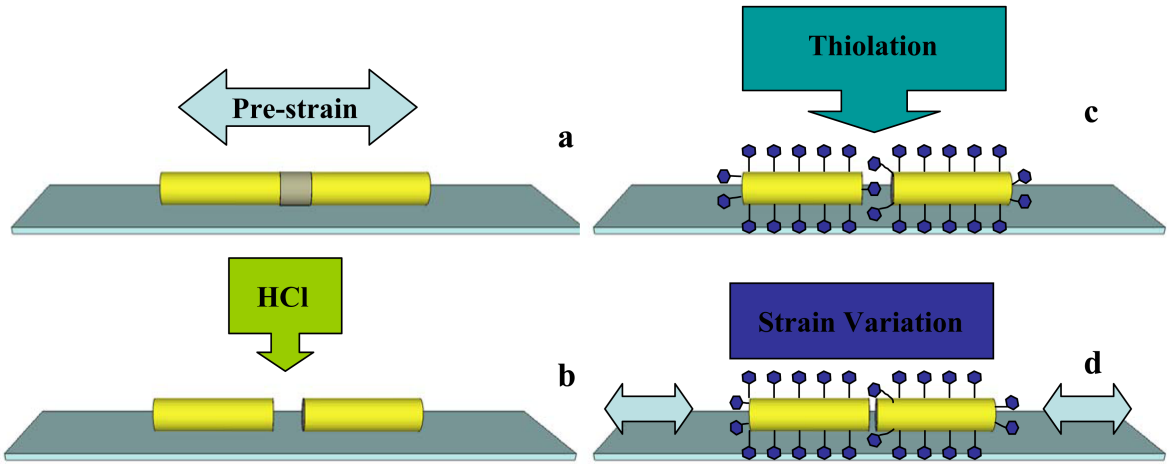

Figure 5.2: A schematic illustration of the dimer fabrication process. (a) Heterogenenous nanorods are deposited on a pre-strained silicone rubber film. (b) An aqueous solution of hydrochloric acid is used to etch away the silver spacer layer. (c) The entire substrate is immersed in a 1 mM ethanolic solution of thiophenol to functionalize the dimer. (d) Substrate strain is varied to move the nanorod segments relative to each other.

5.2.3 Stretching stage fabrication

5.2.4 Gap control through strain varation

Control of the interparticle gap was achieved by modulating the strain of the elastomer substrate using a hysteresis-free translation stage outfitted with a fine micrometer (Fig. 5.2 and 5.3). Strain measurements at the macro- and microscopic levels are known to be linearly proportional and this was verified for the specific case of the samples used in this study by observing changes in separation between nanoparticle pairs in response to substrate deformation. This test was extended to the 300 nm particle-particle length

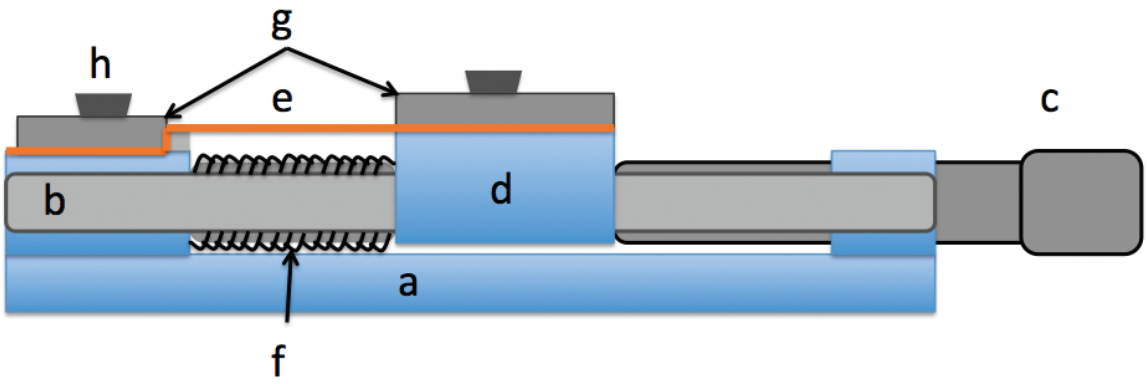

Figure 5.3: Schematic of strain stage: a) aluminum base, b) steel support rail, c) finely threaded thumb-screw, d) steel translation stage mounted on support rails, e) elastomeric substrate, f) counter-spring, g) steel pressure plate (designed to secure elastomer to the stage) h) flathead screw (secures pressure plate over elastomer)

scale, the smallest distances that can reliably be measured with a confocal microscope. Preliminary stretching experiments on 1 μm polystyrene beads deposited on the elastomer reveal a linear relationship between the strain measured at both the macroscopic (i.e. total change in length of the elastomer film) and the microscopic (i.e. change in distance between individual nanoparticles determined through confocal imaging) levels which is presumed to extend down to the molecular scale (see appendix C.2 for a detailed description of this preliminary test).

Unlike isotropic point-like nanoparticles which should, under ideal conditions, only be in contact with the substrate at a single point, the elongated nanorod geometry necessitates the calculation of customized strain-distance scaling factors for each dimer pair. The elongated shaft of the nanorod provides a large area that can potentially be in contact with the substrate when the nanorod is initially deposited on the substrate. When the elastomer is deformed, the rigid nanorod resists deformation and subsequently

detaches from the substrate at all but a single point. The distance between these two points of attachment for each dimer pair determines the linear scaling factor that governs the relationship between the strain applied to the substrate and the actual distance the nanorods move relative to each other. For instance, if two ideal 1 μm cylindrical nanorods aligned end-to-end were both connected to the substrate at the center of their long axes, then the distance between these points of attachment for touching rods would be exactly 1 μm. To open a 5 nm gap between the rods, the distance between these two points would need to be increased to 1005 nm, necessitating a 0.5% strain applied to the substrate. If the length of the elastomeric substrate is 1 cm, this length would need to be increased by 50 μm, a movement that is easily achieved with a micrometer stage. Likewise, to open a clearly visible gap, say 500 nm, the substrate would need to be stretched to 1.5 cm in length, highlighting the necessity of a substrate material with sufficient recoverable strain.

To obtain the customized scaling factors used in these experiments, unetched nanorods were deposited on an elastomeric substrate under sufficient strain to bring individual segments into head-to-head contact upon etching and relaxation of the film. Next, the substrate was immersed in a 6 M aqueous solution of HCl for approximately 10 minutes to dissolve the silver spacer layer and substrate strain was subsequently reduced to bring the particles into physical contact. The substrate was then strained again to create a large (approximately 1000 nm) gap between the nanorods which could be measured optically. This measured distance was then correlated with the change in length of the substrate (measured with the stage micrometer) from which the nanoscopic movements between

the particles could be deduced. Here, it is important to emphasize that because the distance between the points of contact to the substrate are different for every nanorod pair, it was necessary to perform this correlation for every dimer used in this study.

5.2.5 Raman measurements

SERS signal measurements from individual dimers were obtained using The same instrumentation and experimental techniques described in section 4.2.4. The dimers were illuminated by centering the laser spot (diameter $\sim$ 2 μm) over the central gap and spectra were subsequently collected with an integration time of 60 s. Exposure to intense laser radiation can degrade the reporter molecule over time so stability tests were performed to determine a laser power that would allow the signal to remain stable. It was determined that 100 μW measured at the sample surface provided a signal that was sufficiently stable and strong. The dependence of the SERS signal strength on the interparticle spacing was tracked by measuring the Raman signal from an individual nanorod pair repeatedly as the substrate strain was varied with the micrometer in small increments. In order to ensure reproducibility of these experimental results and to further rule out the possibility of data being skewed by laser-induced degradation of the reporter molecule, all measurements were performed over three stretching cycles for each dimer considered here. The results of a typical spectrum for a particle-particle separation of $\sim$ 10 nm is shown in Fig. 5.4. The most pronounced peaks appear at 1000 cm^{-1} (Ring out-of-plane deformation and C-H out-of-plane bending), 1080 cm^{-1} (C-C symmetric stretching and C-S stretching), and 1577 cm^{-1} (C-C symmetric stretching) [21].

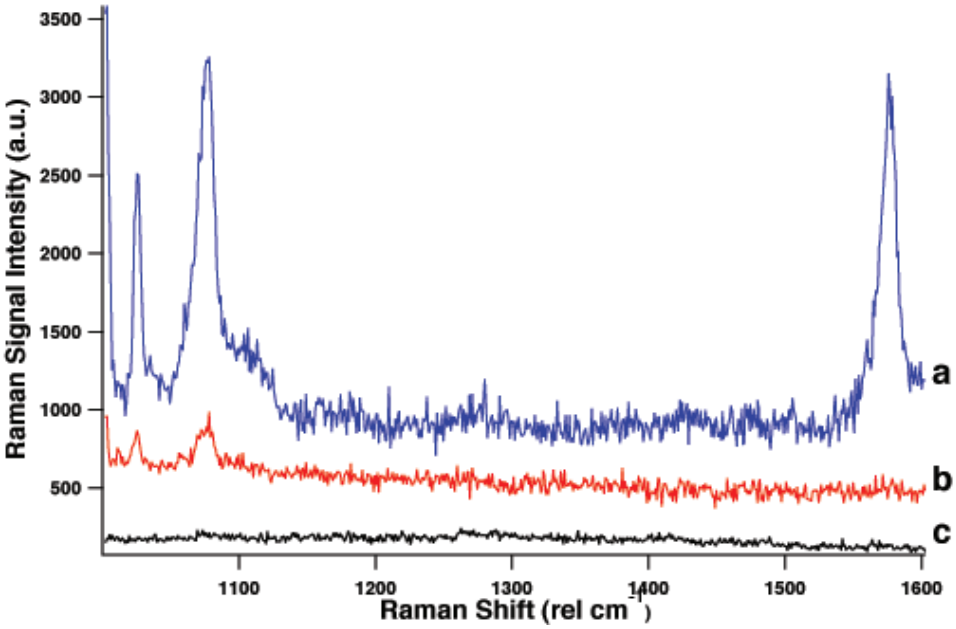

Figure 5.4: (a) A spectrum of a 320 nm diameter nanorod pair functionalized with benzenethiol (approximately 10 nm separation) taken with 785 nm laser light polarized along the dimer axis. (b) A spectrum of the same dimer with light polarized perpendicular to the dimer axis. (c) A spectrum of the same nanorod pair at a separation of 300 nm. Traces are artificially offset for clarity.

5.3 Results and discussion

Normalized data depicting the dependences of the intensity of the Raman band at 1080 cm^{-1} to the dimer gap separation presented in Fig. 5.5 and are in good agreement with theoretical predictions. Here, it should be noted that because the length, width and gap roughness of the dimers used in this study were not identical, the data presented in Fig. 5.5 are only representative of a single dimer. However, data taken from two other dimers displayed trends matching the ones shown here and were in general agreement with the results of the FEM simulations in the sense that they showed enhanced Raman signals at gap distances under 20 nm. Furthermore, to strengthen the argument that the origin of the strong variation in the Raman enhancement is indeed the dispersion of the dimer modes, the extinction spectra were calculated for the nanorod dimer pairs. These results illustrate the tight link between the strength of the enhanced Raman signal and the absorption peaks, which strengthens this claim [2] (see appendix C.1 for further details on the C.3 for measurements of additional nanorod pairs). Finally, it is important to note that one of the limiting factors in this experiment was to find SERS-active nanorod pairs that were aligned with the translational stage axis. Optical tracking of individual structures reveals that dimers not aligned along the direction of applied strain tend to move at some angle to, rather than along, the dimer axis when strain is varied. This changes the morphology of the gap and inhibits accurate assessments of changes in interparticle spacing. For this reason, care was taken to conduct measurements only on nanorod pairs aligned directly along the axis of strain.

Gap estimate error was calculated from the diffraction-limited measurement of the

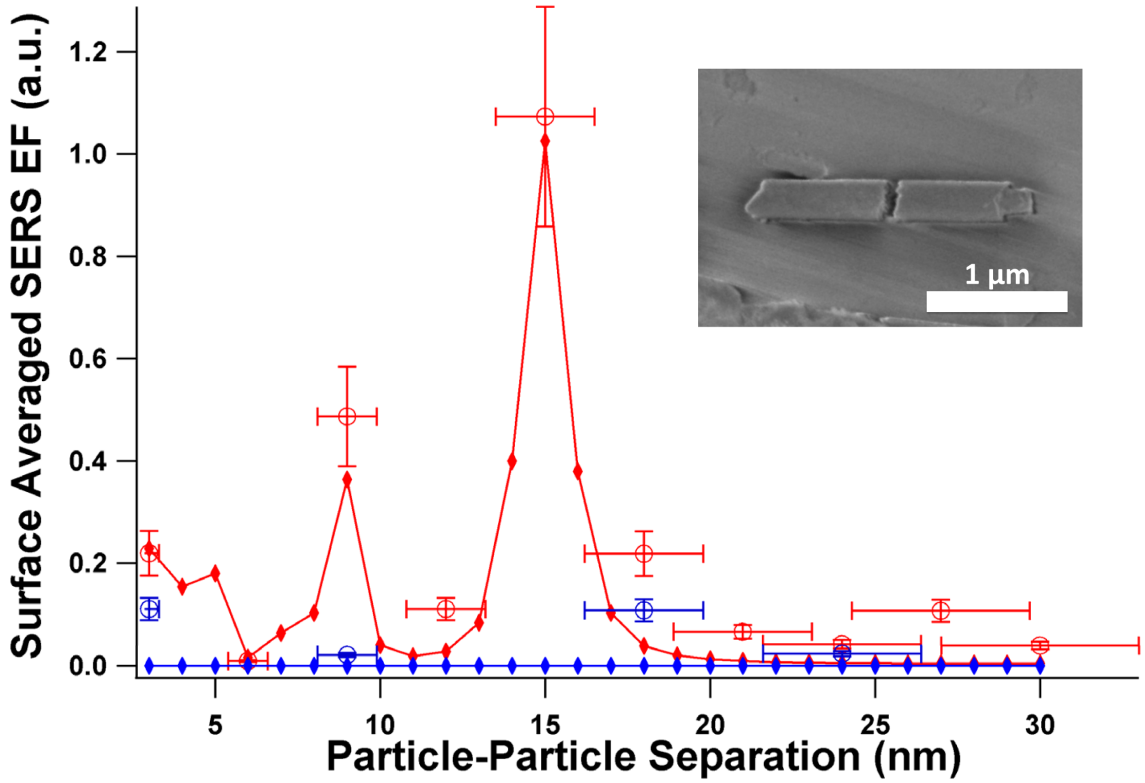

Figure 5.5: Red and blue traces show the calculated values of the surface averaged SERS enhancement factor for polarization parallel and perpendicular to the dimer axis, respectively. Red circles denote the experimental values for the SERS enhancement factor for parallel-to-axis illumination. Blue circles denote experimental values for perpendicular-to-axis illumination. Inset: A SEM image of a typical nanorod pair used in these experiments. Y-error bars calculated from observed dispersion in EF data. X-error bars calculated as described previously. Inset: SEM image of a typical nanorod dimer pair.

relative position of the particles as there is a $\lambda/2$ error determining the distance between them. This measurement was made at the maximum separation of 1000 nm between the rods and, assuming that 400 nm light gives the sharpest image, this yields an uncertainty in the relative position of 20% that carries out to all deduced separation values. Significantly, the largest enhancement observed in the experimental measurements occurs at an interparticle separation of approximately 15 nm, in close agreement with the simulated EF. While the small number of measured points in the data set does not exactly reproduce the simulated EF values, it is nonetheless a strong indication that the true position of the peak is in the vicinity of this particular gap size. This is particularly obvious in the measurements taken from other dimers in this study where the exact height and locations of the peaks are not commensurate with those predicted by FEM. Furthermore, it is also important to note that the dimers in this model are perfect cylinders which do not include surface imperfections, the polycrystalline nature of the segments, or the inherent roughness of the interparticle gap, which would account for the observable SERS signal for perpendicular excitation which was is not predicted by FEM calculations. In a recent study on the structural effects of gap roughness on the SERS enhancement, it was demonstrated that roughened gapped rod pairs exhibited significant resonance broadening from plasmon dephasing that occurs due to protrusions that cause irregularities in interparticle spacing (and, thus, interaction) between segments [57]. As the nanorods used in this study are inherently rough at the interparticle interface, it is very likely that the peak would be smeared across a certain range of interparticle separations.

We have also extended this investigation to include the situation in which the incident

electric field is oriented both parallel and perpendicular to the dimer axis. Previous studies have demonstrated that the sensitivity of the SERS signal to the polarization of the incident radiation was most pronounced at small separations (i.e. when the resultant SERS signal is large) and gradually wanes as particle-particle separation is increased [4, 69]. This is largely due to the fact that, at larger separation distances, the dipole coupling weakens, leaving higher-order resonances which are not necessarily strongly polarization dependent to contribute to the bulk of the measured signal strength. Both the simulation results as well as the experimental findings show a large contrast between polarizations at separations less than 15 nm with this difference becoming smaller at larger interparticle distances, consistent with previous reports.

In conclusion, a facile method to control SERS-active dimer spacing through the fabrication of nanorod heterostructures on elastomeric substrates was developed. Subsequent measurements of the SERS enhancement factor over a range of interparticle separations yielded a trend consistent with what was predicted by FEM simulations for primary mode resonances. This method improves upon methods proposed in recent publications [22] because the ideal interstitial spacing can effectively be designed into the nanorod growth process, eliminating the need for excessive tuning to bring the dimer into resonance. This is an important advantage for potential scientific and commercial applications of this technique, as it reduces the need for excessive particle movement to produce large SERS enhancement factors. Furthermore, since every heterostructure can be made into a nanorod dimer, this technique provides a high-throughput, consistent and tunable means by which SERS-active structures can be created. This technique can be

extended to probe more complex structures such as nanoparticle chains and plasmonic coupling between nanoparticles of different materials.

Chapter 6

Conclusions

In this dissertation, I have sought to build an understanding of the roles metal nanoparticle dimers play in SERS research. The desire to build ultra-sensitive chemical sensors for trace analyte detection drives the current interest in the development of SERS-active substrates. However, lack of reproducibility of enhancement factors, the limitations of current lithographic equipment, and difficulties in devising experiments to further our understanding of the SERS process have greatly inhibited the development of a SERS substrate capable of truly large EFs. While advancements are being made in the field, a thorough understanding of the SERS enhancement mechanism for specific geometries achieved by *both* theoretical and experimental means is necessary to proceed in the most efficient and practical manner possible.

I have focused on the experimental verification of theoretical predictions regarding the behavior of SERS hot spots in metal nanoparticle dimers. Hot spots in gaps between closely spaced nanoparticles of various sizes and shapes have consistently been identified as the configuration most likely to yield EFs large enough to detect analytes on the single molecule level. However, the sensitivity of the SERS EF to a long list of parameters

coupled with the minute volume of hot spots places these small nanoparticle clusters among the most unpredictable SERS-active structures with respect to EF reproducibility. This fact alone highlights the need experimental analysis of dimers that is complementary to the surfeit of theoretical results already present in the literature.

In the first experimental section of this dissertation, I described the combined use of a soft-lithography-based templating method combined with a capillary force deposition technique to produce nanosphere clusters of various shapes and sizes in a high-throughput manner. Reproducible template patterning was confirmed over areas as large as a 6" silicon wafer and dimer patterning was deemed successful over a 30 $\times$ 30 μm area. The most significant advantage of this technique is the ability to create large numbers evenly-spaced morphologically-similar clusters which can then be used to investigate hot spot behavior. In the experiments conducted in this first experimental section, the ability to create large numbers of hot spots exhibiting EFs as large as 10^9 through observation of the polarization dependence of the interparticle coupling of nanoparticle LSPRs and the resulting gap plasmon was confirmed. In addition, the attempt was made to control interparticle spacing through displacement of the sodium citrate capping agent with a molecule of known molecular and bonding length (benzenethiol). Although this did afford closely-spaced nanoparticle dimers with the reporter molecule located in the hot spot, the fact that parameters such as molecular coverage and the fact that the dimers were not actually linked means that the true interparticle separation for each individual dimer can only be speculated. If spacing is to truly be known, an approach to particle spacing similar to the one implemented by Moskovits *et al.* [47] is necessary. In this approach,

Moskovits exposes silver nanoparticles immobilized on a silicon substrate to a dilute solution of 1-4, benzenedithiol. Following the ligand functionalization, a solution of silver nanoparticle colloid is washed over the particles in a concentration low enough to create dimers connected by a single thiol molecule. Knowing the bond length and the molecule size, this method enables one to ascertain the interparticle distance, at least to a greater degree than can be achieved than by relying on the capillary force alone. If monodisperse nanoparticle "dumbbells" could be created in large quantities, molecular linkers could presumably be used to enhance the results of this particular experiment. However, recent reports on progress in molecularly linked nanoparticle clusters cite problems with monodispersity which, to date, have yet to be solved.

In the second experimental section, I extended the application of the capillary force deposition technique to longer nanoparticle chains in an attempt reconcile conflicting theoretical and experimental results related to enhancement factors - specifically, to answer the question of whether the use of longer chain-lengths could possibly provide enhancement factors that significantly exceed that of the dimer. After taking an in-depth look at the SERS EFs arising from nanoparticle chains ranging 1-9 nanoparticles in length, it was concluded that, although larger enhancement arising from plasmon coupling between multiple particles could, in fact, yield larger surface-averaged SERS EFs than the dimer, these enhancements were not sufficiently larger to merit the extra effort required for making a more complex nanostructure.

Although this is a negative result, this experiment succeeds in making a valid comparison between theoretical and experimental results and demonstrates that these two

entities don't necessarily have to agree. Numerical simulations are, and will continue to be, a valid tool for predicting the outcome of experimental setups before the actual experiments have been performed. As such, these simulations can serve as a useful guide in tailoring experiments and, perhaps most importantly, avoiding wasted time on approaches that are not theoretically viable. However, it is important to note that a simulation is only as accurate as its ability to imitate the thing that it is modeling and, in many cases, the real-life scenario is significantly more complex than what can be accounted for in a computer model. This is of most relevance in the case of SERS hot spots, where it is presently neither possible nor practical to computationally account for every morphological variation, even in a structure as simple as the dimer.

In the final experimental section, I address the possibility of creating an environment in which the SERS response can be manually controlled. Specifically, the particle-particle separation in gold nanorod dimers was varied on the nanoscale using an elastomeric substrate. Because several gap sizes could be created for a single particle pair, the dependence of the SERS EF on interparticle separation could be studied without having to be concerned with the many parameters to which the EF is sensitive. This is an incredibly useful tool, as it provides a means of precisely tuning nanoparticle morphology as well as a way to push past inter-feature separation barriers imposed by the limitations of current lithographic equipment. Another interesting aspect of this technique is the fact that it can be applied to 2-D manipulation of particles. Depending on how the substrate is deformed, it is possible to *rotate* as well as change the spacing between asymmetric nanoparticles such as nanorods. Ideally, this could be implemented in experiments where the plasmonic

coupling between nanoparticles changes with relative contact angle or, more broadly, as a means of fine-tuning the placement of particles that are "almost" in the right position. One particular case where this would be very relevant is in the work done by Funston *et al.* where the plasmonic coupling between closely-spaced gold nanorods is measured for several different geometries.[12] In this experiment, the researchers search for particles in a desired orientation from among a jumble of randomly dispersed nanoparticles. Clearly, the ability to "nudge" particles into a specific position would have greatly facilitated the location clusters suitable for their experiments.

Appendix A

The Raman polarizability tensor and the radiation profile

The Raman polarizability, $\hat{\alpha}$, is a second rank tensor with the important role of defining the linear relationship between **p** and **E**. In Cartesian coordinates, $\hat{\alpha}$ can be expressed as a 3×3 matrix as follows:

$$\begin{pmatrix} p_{\mathrm{x}} \\ p_{\mathrm{y}} \\ p_{\mathrm{z}} \end{pmatrix} = (L_{\mathrm{M}})^{1/4} \begin{pmatrix} \alpha_{\mathrm{xx}} & \alpha_{\mathrm{xy}} & \alpha_{\mathrm{xz}} \\ \alpha_{\mathrm{yx}} & \alpha_{\mathrm{yy}} & \alpha_{\mathrm{yz}} \\ \alpha_{\mathrm{zx}} & \alpha_{\mathrm{zy}} & \alpha_{\mathrm{zz}} \end{pmatrix} \begin{pmatrix} E_{\mathrm{x}} \\ E_{\mathrm{y}} \\ E_{\mathrm{z}} \end{pmatrix} \tag{A.1}$$

The purpose for tensorial expression of $\hat{\alpha}$ arises from the fact that the induced dipole might not be in the same direction as the electric field which is a direct result of the morphology of the analyte molecule and, as a result, each of the nine components are deemed necessary to define the differences in the polarizability direction and strength in different directions. There are special cases, however, in which the Raman polarizability tensor can be simplified. For instance, if **E** is applied along a direction of might molecular symmetry, the induced dipole will generally usually point in approximately the same direction. If this is, in fact, the case, then a new set of axes (x', y', z') can be defined, which allows $\hat{\alpha}$ to be diagonalized as follows:

$$\begin{pmatrix} p_{x'} \\ p_{y'} \\ p_{z'} \end{pmatrix} = (L_M)^{1/4} \begin{pmatrix} \alpha_{x'x'} & 0 & 0 \\ 0 & \alpha_{y'y'} & 0 \\ 0 & 0 & \alpha_{z'z'} \end{pmatrix} \begin{pmatrix} E_{x'} \\ E_{y'} \\ E_{z'} \end{pmatrix} \tag{A.2}$$

Here, it is important to note that the dipole induced by **E** depends not just on the polarizability inherent to the analyte of interest, but also on the orientation of the molecule with respect to the excitation source. As a result, the orientation of the excitation source with respect to the molecule of interest plays a critical role with respect to how strong the resulting Raman signal will be. As such, there are three important special cases that merit a brief overview, as most approaches to defining the power radiated per unit solid angle can be classified into one of them.

A.1 Isotropic polarizability tensor

Here we begin with the most simple of all situations - the case in which the Raman tensor is isotropic (i.e. it does not depend on the orientation of the molecule with respect to the incident beam $\mathbf{E}_{Inc}$). Although this is relatively uncommon, there are a few molecules for which this example applies (e.g. the CCl_4 molecule). Under these conditions, the lack of dependence on the incident beam direction allows the Raman polarizability tensor $\hat{\alpha}$ to be expressed as a constant, α, and subsequently, for the induced Raman dipole to be expressed as $\mathbf{p}_R = (L_M)^{1/4}\alpha\mathbf{E}_{Inc}$. As a result, the radiation profile can be reduced to the following expression:

$$\frac{dP_{\mathrm{Rad}}}{d\Omega}(\theta = 90^{\circ}) = \frac{\omega_{\mathrm{R}}^{4} n_{\mathrm{M}}}{32\pi^{2}\epsilon_{0}c^{3}} L_{\mathrm{M}} |\alpha|^{2} |\mathbf{E}_{\mathrm{Inc}}|^{2} \tag{A.3}$$

where the signal is collected in the commonly used 90° back-scattering configuration.

A.2 Fixed-orientation

In the case where a molecule whose orientation is fixed, $\hat{\alpha}$ cannot be reduced to a constant and the directions of the incident beam and the orientation of a polarizer (if present) play significant roles in how much Raman signal is detected. Under these circumstances, the induced Raman dipole is expressed as $\mathbf{p}_{\mathrm{R}} = (L_{\mathrm{M}})^{1/4}\hat{\alpha}\mathbf{E}_{\mathrm{Inc}}$ and $\mathbf{e}_{\mathrm{Inc}}$. Now, if $\mathbf{e}_{\mathrm{P}}$ denote the unit vectors along the directions of polarization of the incident beam and the polarizer, respectively, the radiation profile can be expressed as:

$$\frac{dP_{\mathrm{Rad}}}{d\Omega}(\theta = 90^{\circ}) = \frac{\omega_{\mathrm{R}}^{4} n_{\mathrm{M}}}{32\pi^{2}\epsilon_{0}c^{3}} L_{\mathrm{M}} |\mathbf{e}_{\mathrm{P}} \cdot \hat{\alpha} \cdot \mathbf{e}_{\mathrm{Inc}}|^{2} |\mathbf{E}_{\mathrm{Inc}}|^{2} \tag{A.4}$$

where the signal is, again, assumed to be detected using the 90° back-scattering configuration.

A.3 Orientation-averaging

In experiments involving large numbers of randomly oriented molecules, it statistically probable that the Raman signal measured is an average over all possible molecular orientations. In this situation, it makes sense to apply a method of averaging to the

polarizability tensor in order to reflect this. Depending on the choice of polarization for the incident beam and the relative polarization of the detection setup, the results can be quite different thus a brief explanation of the radiation profiles for detection parallel and perpendicular to $\mathbf{E}_{\mathrm{Inc}}$ are included here.

Consider an incident excitation along $\mathbf{e}_{\mathrm{x}}$ with $\mathbf{E}_{\mathrm{Inc}}$ having polarization $\mathbf{e}_{\mathrm{Inc}} = \mathbf{e}_{\mathrm{z}}$. The radiation profile is given as:

$$\frac{dP^{\parallel}_{\mathrm{Rad}}}{d\Omega}(\theta = 90^{\circ}) = \frac{\omega^4_{\mathrm{R}} n_{\mathrm{M}}}{32\pi^2 \epsilon_0 c^3} L_{\mathrm{M}} \langle |\mathbf{e}_{\mathrm{z}} \cdot \hat{\alpha} \cdot \mathbf{e}_{\mathrm{z}}|^2 | \rangle |\mathbf{E}_{\mathrm{Inc}}|^2 \tag{A.5}$$

Similarly, for the case where the incident polarization is perpendicular to the detection polarization (i.e. $\mathbf{e}_{\mathrm{Inc}} = \mathbf{e}_{\mathrm{y}}$, we have:

$$\frac{dP^{\parallel}_{\mathrm{Rad}}}{d\Omega}(\theta = 90^{\circ}) = \frac{\omega^4_{\mathrm{R}} n_{\mathrm{M}}}{32\pi^2 \epsilon_0 c^3} L_{\mathrm{M}} \langle |\mathbf{e}_{\mathrm{y}} \cdot \hat{\alpha} \cdot \mathbf{e}_{\mathrm{z}}|^2 | \rangle |\mathbf{E}_{\mathrm{Inc}}|^2 \tag{A.6}$$

where $\langle ... \rangle$ denotes the averaging over the random orientation of the molecules.

Now, it is easy to assume that the information provided by the polarizability tensor would be averaged out by this process. However, $\mathbf{e}_{\mathrm{y}}$ and $\mathbf{e}_{\mathrm{z}}$ remain dependent on the intrinsic symmetry invariants of $\hat{\alpha}$. When the averages are carried out, we have:

$$\begin{cases} \langle |\mathbf{e}_{\mathrm{z}} \cdot \hat{\alpha} \cdot \mathbf{e}_{\mathrm{z}}|^2 \rangle = (45\bar{\alpha}^2 + 4\bar{\gamma}^2)/45 \\ \langle |\mathbf{e}_{\mathrm{y}} \cdot \hat{\alpha} \cdot \mathbf{e}_{\mathrm{z}}|^2 \rangle = 3\bar{\gamma}^2/45 \end{cases} \tag{A.7}$$

where,

$$\bar{\alpha} = \frac{1}{3}[\alpha_{xx} + \alpha_{yy} + \alpha_{zz}] \tag{A.8}$$

$$\bar{\gamma}^2 = \frac{1}{2}[(\alpha_{xx} - \alpha_{yy})^2 + (\alpha_{yy} - \alpha_{zz})^2] + 3[\alpha_{xy}^2 + \alpha_{xz}^2 + \alpha_{yz}^2] \tag{A.9}$$

which are termed the 'reduced trace' and the 'anisotropy' of the tensor, respectively. These quantities can be substituted into A.7 and then used to solve for A.5 and A.6 as needed.

Appendix B

Formal definition of the local field correction L_{M}

As mentioned in section 1.2.2, the electromagnetic response of the medium the analyte is embedded in/near results in the microscopic fields immediately at the molecule to vary distinctly from the average macroscopic field in the area around it. In order to correct for this in calculations of the Raman polarizability, it is necessary to introduce a local field correction factor, L_{M}. This is of particular importance for Raman measurements taken in liquids, due to the presence of surrounding solvent. However, this correction also plays an important role in SERS, where the presence of a molecular monolayer over a metallic surface can also alter the microscopic fields. The derivation of this factor is discussed in detail in reference [23], but a brief sketch is provided here.

The field felt by the analyte from the medium arises from the contributions of: (1) the field from external charges, $\mathbf{E}_{\mathrm{ext}}$ and, (2) from the internal charges in the medium $\mathbf{E}_{\mathrm{int}}$. In order to obtain the microscopic field, $\mathbf{E}_{\mathrm{micro}}$, it is necessary to subtract the macroscopic internal contribution $\mathbf{E}_{\mathrm{int}}$ and substitute the microscopic field arising from the local environment, $\mathbf{E}_{\mathrm{close}}$(i.e. the few molecules/atoms immediate vicinity of the analyte):

$$\mathbf{E}_{\mathrm{micro}} = \mathbf{E} - \mathbf{E}_{\mathrm{int}} + \mathbf{E}_{\mathrm{close}} \tag{B.1}$$

where $\mathbf{E}$ is the macroscopic field derived from Maxwell's equations. $\mathbf{E}_{\text{int}}$ can thus be described as coming from the fields created by the macroscopic polarization of the embedding medium immediately around the analyte:

$$\mathbf{E}_{\text{int}} = -\frac{1}{3\epsilon_0}\mathbf{P} \tag{B.2}$$

$\mathbf{E}_{\text{close}}$ is, by no means, easy to estimate, as it is completely dependent on local symmetries in the environment and the analyte molecule itself. In a highly symmetric environment like the cubic lattice in a crystal, $\mathbf{E}_{\text{close}}$ vanishes completely. Similarly, in a completely random environment as in the case of a liquid embedding medium, $\mathbf{E}_{\text{close}} \sim 0$.

Next, combining the well established relation $\mathbf{P} = \epsilon_0(\epsilon_{\text{M}} - 1)$ and substituting it into equation B.2, we arrive at:

$$\mathbf{E}_{\text{micro}} = \frac{\epsilon_{\text{M}} + 2}{3}\mathbf{E} \tag{B.3}$$

which links the microscopic electric field that is felt by the analyte to the macroscopic electric field we are familiar with from Maxwell's equations. Now, referring back to equation 1.4 in in chapter 1, we know that:

$$\mathbf{E}_{\text{micro}} = (L_{\text{M}})^{1/4}\mathbf{E}_{\text{macro}} \tag{B.4}$$

with the power of 1/4 originating from the expression of the Raman cross-section [71]. Applying equation B.3 to equation B.4 gives us the expression already stated in section 1.2.2, namely:

$$(L_{\mathrm{M}})^{1/4} = \frac{\epsilon_{\mathrm{M}} + 2}{3} \tag{B.5}$$

Appendix C

Supplementary information for interparticle gap tuning

C.1 Extinction spectrum simulations for gold nanorod dimers

In Fig. C.1 we have calculated the extinction, scattering and absorption spectra for gold nanorod dimers of diameter 320 nm, comprised of segments 400, 600 and 800 nm in length and with gap sizes 9, 12, and 15 nm wide. Our results indicate that the scattering from these large nanoparticles presents a broad, almost featureless spectrum due to the excitation of higher order modes. The computer model also allows us to compare the scattering magnitude with that of the absorption. Here, our results suggest that the enhancement factor is exclusively dependent on the absorption part of the nanorod extinction spectrum, rather than the scattering which is the bulk contributor to the nanorod extinction.

C.2 Correlation between macro- and microscopic strain

We performed strain measurements on 1 μm diameter polystyrene beads to test the validity of the strain-scaling technique used in these experiments. Specifically, we aimed

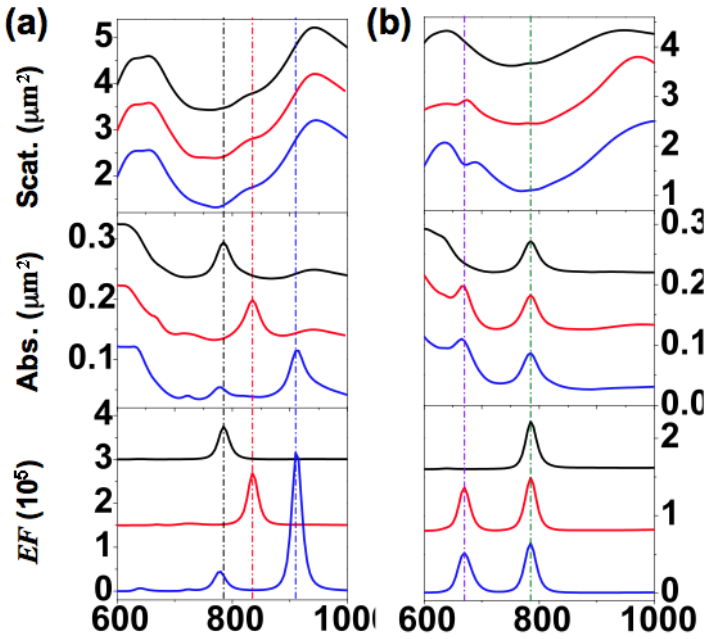

Figure C.1: Scattering (top), absorption (middle) and Raman enhancement factor EF (bottom) for Au rod dimers, (a) for different gap distances: 15 nm (black), 12 nm (red) and 9 nm (blue) and, (b) for different segment length: 400 nm (black), 600 nm (red) and 800 nm (blue). The Raman enhancement peaks always correspond to the absorption peaks, but not necessarily the scattering peak. The segment length L = 1 μm in (a) were unchanged, and the gap in (b) were kept at 15 nm. Diameters of rods were 320 nm in both (a) and (b).

to check if the $Strain = \frac{\Delta L}{L}$ relation breaks down for any reason (e.g. substrate failure, particle delamination, etc.) above the length scale relevant for our dimer stretching experiments. The polystyrene beads were applied to the substrate which was subsequently imaged in dark field (scattering) mode with a 150× objective. Bead pairs that were located along the same line of strain were identified and imaged with a high resolution camera as the applied strain was varied. Images of the displaced bead pairs were processed in ImageJ to measure the change in distance resulting from each level of applied strain. These measurements we repeated three times and the results were averaged. This experimentally measured "microscopic" strain was plotted against the strain extrapolated from the measured change in length of the substrate as measured by a micrometer (Fig. C.2). Our results yielded a nearly 1:1 correlation, suggesting that the relation remains valid in the vicinity of the length scale of interest.

C.3 Additional SERS experimental results and comparison with simulations

In Fig C.3 we present additional examples of gap size vs EF measurements taken from other nanorod pairs in this study. All calculated data was taken from Fig. 5.1 in the main text. Of particular interest here is the SERS enhancement peak in Fig C.3a which is noticeably different from the simulated results. As we have already shown in our simulations, the location of the maximum SERS enhancement is sensitive to nanorod diameter (Fig. 5.1a in main text) and it possible that a difference in size could have

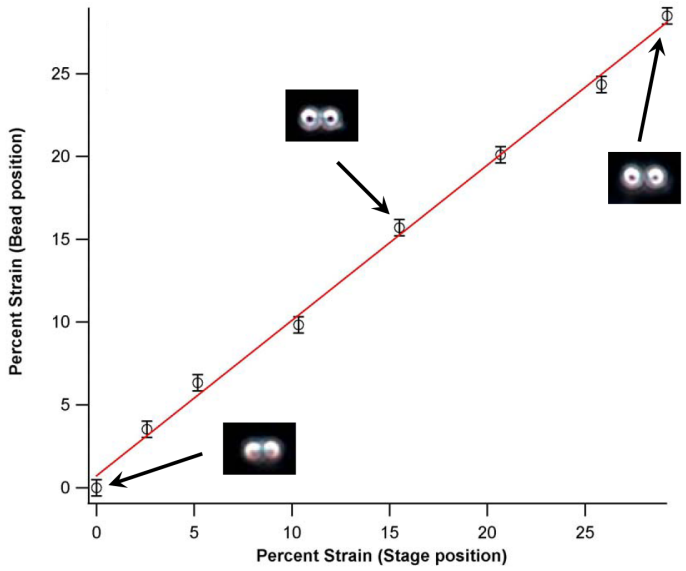

Figure C.2: The trace is this figure depicts the correlation between the macroscopic strain applied to the elastomer substrate (measured with a micrometer) and the microscopic strain measured between polystyrene beads (deduced through digital image analysis). Error bars were calculated from standard error

contributed to this discrepancy. However, there are other features of the geometry of the nanorods used in this experiment that are not accounted for (gap roughness, for instance), so further investigation would be necessary to provide confirmation of this.

Finally, figure C.4 shows EF measurements where very large gap sizes have been taken into account. This figure illustrates that when the two nanorods are separated by a distance greater than 30 nm, the magnitude of the EF drops to and remains at approximately zero. This finding agrees well with electromagnetic theory which suggests that the largest SERS enhancements for a nanoparticle dimer system like the one presented here occurs when the two nanoparticles are close enough to couple through near-field interactions.

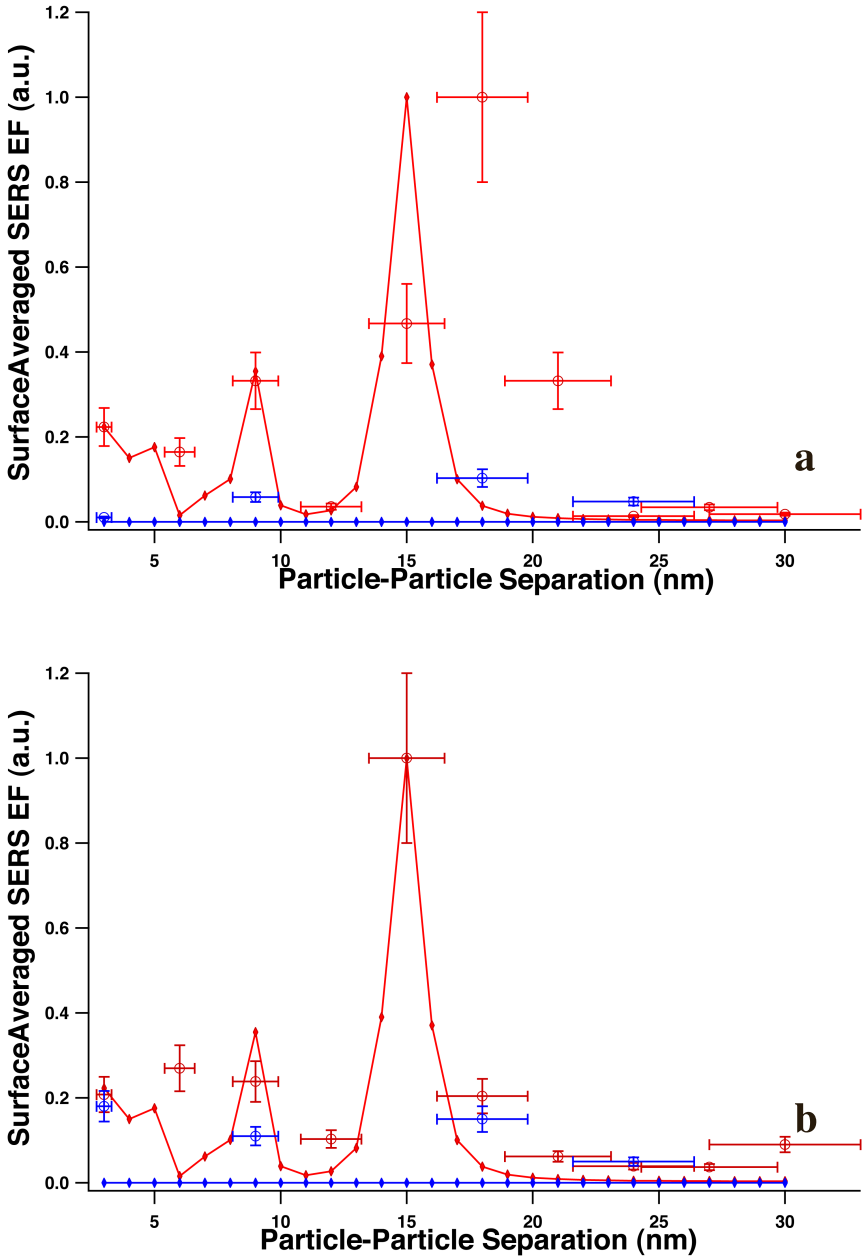

Figure C.3: Figures (a) and (b) show experimental data (red and blue circles denoting measurements made parallel and perpendicular to the dimer axis, respectively) taken from two dimer pairs with segments approximately 320 nm in diameter, plotted against the results from FEM simulations (red and blue traces denoting results from parallel and perpendicularly polarized illumination, respectively). Error bars were calculated from the dispersion of the data observed during measurements.

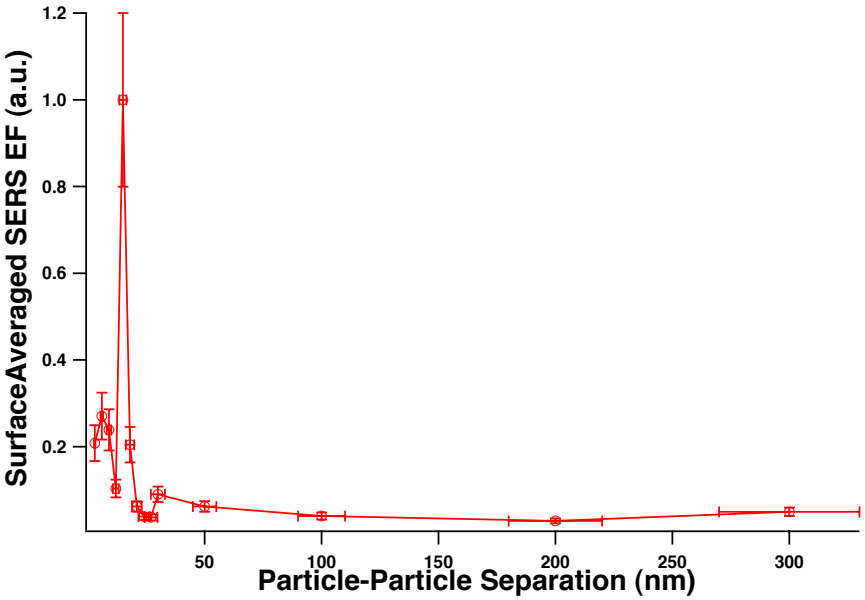

Figure C.4: Experimental measurements of the surface averaged SERS EF (normalized) plotted against interparticle separation with additional measurements of the EF taken at separations ranging from 30-300 nm to demonstrate that the value remains stable around zero for separations larger than approximately 30 nm.

Bibliography

[1] K. D. Alexander, M. J. Hampton, S. P. Zhang, A. Dhawan, H. X. Xu, and R. Lopez. A high-throughput method for controlled hot-spot fabrication in sers-active gold nanoparticle dimer arrays. *Journal of Raman Spectroscopy*, 40(12):2171–2175, 2009.

[2] K. D. Alexander, K. Skinner, S. P. Zhang, H. Wei, and R. Lopez. Tunable sers in gold nanorod dimers through strain control on and elastomeric substrate. *Nano Letters*, 10(11):4488–4493, 2010.

[3] K. D. Alexander, S. P. Zhang, A. R. Hight Walker, H. X. Xu, and R. Lopez. An investigation of the relationship between length and sers enhancement in metal nanoparticle chains. 2011. Submitted to The Journal of Raman Spectroscopy.

[4] M. J. Banholzer, S. Z. Li, J. B. Ketter, D. I. Rozkiewicz, G. C. Schatz, and C. A. Mirkin. Electrochemical approach to and the physical consequences of preparing nanostructures from gold nanorods with smooth ends. *Journal of Physical Chemistry C*, 112(40):15729–15734, 2008.

[5] L. C. Brousseau, J. P. Novak, S. M. Marinakos, and D. L. Feldheim. Assembly of phenylacetylene-bridged gold nanocluster dimers and trimers. *Advanced Materials*, 11(6):447–+, 1999.

[6] W. B. Cai, B. Ren, X. Q. Li, and et al. Investigation of surface enhanced raman scattering from platinum electrodes using a confocal raman microscope: dependence of surface roughening pretreatment. *Surface Science*, 406:406–409, 1998.

[7] Y. Cui, M. T. Bjork, J. A. Liddle, C. Sonnichsen, B. Boussert, and A. P. Alivisatos. Integration of colloidal nanocrystals into lithographically patterned devices. *Nano Letters*, 4(6):1093–1098, 2004.

[8] N. V. Dziomkina and G. J. Vancso. Colloidal crystal assembly on topologically patterned templates. *Soft Matter*, 1(4):265–279, 2005.

[9] L. E. Euliss, J. A. DuPont, S. Gratton, and J. M. DeSimone. Imparting size, shape, and composition control of materials for nanomedicine. *Chemical Society Reviews*, 35(11):1095–1104, 2006.

[10] Y. Fang, H. Wei, F. Hao, P. Nordlander, and H. X. Xu. Remote-excitation surface-enhanced raman scattering using propagating ag nanowire plasmons. *Nano Letters*, 9(5):2049–2053, 2009.

[11] S. Foteinopoulou, J. P. Vigneron, and C. Vandenbem. Optical near-field excitations on plasmonic nanoparticle-based structures. *Optics Express*, 15(7):4253–4267, 2007.

[12] A. M. Funston, C. Novo, T. J. Davis, and P. Mulvaney. Plasmon coupling of gold nanorods at short distances and in different geometries. *Nano Letters*, 9(4):1651–1658, 2009.

[13] M. Futamata, Y. Maruyama, and M. Ishikawa. Local electric field and scattering cross section of ag nanoparticles under surface plasmon resonance by finite difference time domain method. *Journal of Physical Chemistry B*, 107(31):7607–7617, 2003.

[14] B. D. Gates, Q. B. Xu, M. Stewart, D. Ryan, C. G. Willson, and G. M. Whitesides. New approaches to nanofabrication: Molding, ing, and other techniques. *Chemical Reviews*, 105(4):1171–1196, 2005.

[15] J. M. Gerardy and M. Ausloos. Absorption spectrum of clusters of spheres from the general solution of maxwell's equations. ii. optical properties of aggregated metal spheres. *Physical Review B*, 25:4204–4229, 1982.

[16] A. Gopinath, S. V. Boriskina, W. R. Premasiri, L. Ziegler, B. M. Reinhard, and L. Dal Negro. Plasmonic nanogalaxies: Multiscale aperiodic arrays for surface-enhanced raman sensing. *Nano Letters*, 9(11):3922–3929, 2009.

[17] Stephanie E. A. Gratton, Stuart S. Williams, Mary E. Napier, Patrick D. Pohlhaus, Zhilian Zhou, Kenton B. Wiles, Benjamin W. Maynor, Clifton Shen, Tove Olafsen, Edward T. Samulski, and Joseph M. DeSimone. The pursuit of a scalable nanofabrication platform for use in material and life science applications. *Accounts of Chemical Research*, 41(12):1685–1695, 2008.

[18] L. Gunnarsson, E. J. Bjerneld, H. Xu, S. Petronis, B. Kasemo, and M. Kall. Interparticle coupling effects in nanofabricated substrates for surface-enhanced raman scattering. *Applied Physics Letters*, 78(6):802–804, 2001.

[19] L. Gunnarsson, T. Rindzevicius, J. Prikulis, B. Kasemo, M. Kall, S. L. Zou, and G. C. Schatz. Confined plasmons in nanofabricated single silver particle pairs: Experimental observations of strong interparticle interactions. *Journal of Physical Chemistry B*, 109(3):1079–1087, 2005.

[20] E. Hao and G. C. Schatz. Electromagnetic fields around silver nanoparticles and dimers. *Journal of Chemical Physics*, 120(1):357–366, 2004.

[21] J. W. Hu, B. Zhao, W. Q. Xu, Y. G. Fan, B. Li, and Y. Ozaki. Simple method for preparing controllably aggregated silver particle films used as surface-enhanced raman scattering active substrates. *Langmuir*, 18(18):6839–6844, 2002.

[22] Fumin Huang and Jeremy J. Baumberg. Actively tuned plasmons on elastomerically driven au nanoparticle dimers. *Nano Letters*, 10(5):1787–92, 2010.

[23] J. D Jackson. *Classical electrodynamics*. Wiley, New York, 1998.

[24] P. K. Jain and M. A. El-Sayed. Surface plasmon coupling and its universal size scaling in metal nanostructures of complex geometry: Elongated particle pairs and nanosphere trimers. *Journal of Physical Chemistry C*, 112(13):4954–4960, 2008.

[25] D. L. Jeanmaire and R. P. Vanduyne. Surface raman spectroelectrochemistry .1. heterocyclic, aromatic, and aliphatic-amines adsorbed on anodized silver electrode. *Journal of Electroanalytical Chemistry*, 84(1):1–20, 1977.

[26] J. Jiang, K. Bosnick, M. Maillard, and L. Brus. Single molecule raman spectroscopy at the junctions of large ag nanocrystals. *Journal of Physical Chemistry B*, 107(37):9964–9972, 2003.

[27] J. Jin. *The finite element method in electromagnetics*. Wiley-IEEE Press, New York, 2002.

[28] P. Johansson, H. Xu, and M. Kall. Surface-enhanced raman scattering and fluorescence near metal nanoparticles. *Physical Review B*, 72, 2005.

[29] B. Johnson and R. W. Christy. Optical constants of noble metals. *Physical Review B*, 6:4370–4379, 1972.

[30] P. Kambhampati, C. M. Child, M. C. Foster, and A. Campion. On the chemical mechanism of surface enhanced raman scattering: Experiment and theory. *Journal of Chemical Physics*, 108(12):5013–5026, 1998.

[31] K. L. Kelly, E. Coronado, L. L. Zhao, and G. C. Schatz. The optical properties of metal nanoparticles: The influence of size, shape, and dielectric environment. *Journal of Physical Chemistry B*, 107(3):668–677, 2003.

[32] W. Kiefer. Recent advances in linear and nonlinear raman spectroscopy. *Journal of Raman Spectroscopy*, 38:1538–1553, 2007.

[33] K. Kneipp, Y. Wang, H. Kneipp, L. T. Perelman, I. Itzkan, R. Dasari, and M. S. Feld. Single molecule detection using surface-enhanced raman scattering (sers). *Physical Review Letters*, 78(9):1667–1670, 1997.

[34] J. Koch, K. Grun, M. Ruff, R. Wernhardt, and A. D. Wieck. Creation of nanelectronic devices by focussed ion beam implantation. *Industrial Electronics Society, 1999, IECON '99 Proceedings*, 1:35–39, 1999.

[35] J. T. Krug, G. D. Wang, S. R. Emory, and S. M. Nie. Efficient raman enhancement and intermittent light emission observed in single gold nanocrystals. *Journal of the American Chemical Society*, 121(39):9208–9214, 1999.

[36] K. Kunz and R. Luebbers. *The finite difference time-domain method for electromagnetics*. CRC press, Boca Raton, FL, 1993.

[37] E. C. Le Ru and P. G. Etchegoin. *Principles of Surface-Enhanced Raman Spectroscopy and Related Plasmonic Effects*. Elsevier, Amsterdam, 2009.

[38] E. C. Le Ru, P. G. Etchegoin, and M. and Meyer. Enhancement factor distribution around a single surface-enhanced raman scattering hot spot and its relation to single molecule detection. *Journal of Physical Chemistry C*, 111:16076–16079, 2007.

[39] S. J. Li, D. Y. Wu, X. Y. Xu, and R. N. Gu. Theoretical and experimental studies on the adsorption behavior of thiophenol on gold nanoparticles. *Journal of Raman Spectroscopy*, 38:1436–1443, 2007.

[40] Shuzhou Li, Maria L. Pedano, Shih-Hui Chang, Chad A. Mirkin, and George C. Schatz. Gap structure effects on surface-enhanced raman scattering intensities for gold gapped rods. *Nano Lett*, 10(5):1722–7, 2010.

[41] J. Lu, D. Chamberlin, D. A. Rider, M. Z. Liu, I. Manners, and T. P. Russell. Using a ferrocenylsilane-based block copolymer as a template to produce nanotextured ag surfaces: uniformly enhanced surface enhanced raman scattering active substrates. *Nanotechnology*, 17(23):5792–5797, 2006.

[42] B. W. Maynor, I. Larue, Z. Hu, J. P. Rolland, A. Pandya, Q. Fu, J. Liu, R. J. Spontak, S. S. Sheiko, R. J. Samulski, E. T. Samulski, and J. M. DeSimone. Supramolecular nanomimetics: Replication of micelles, viruses, and other naturally occurring nanoscale objects. *Small*, 3(5):845–849, 2007. Maynor, Benjamin W. LaRue, Isaac Hu, Zhaokang Rolland, Jason P. Pandya, Ashish Fu, Qiang Liu, Jie Spontak, Richard J. Sheiko, Sergei S. Samulski, Richard J. Samulski, Edward T. DeSimone, Joseph M.

[43] J. M McMahon, A. I Henry, K. L. Wustholtz, M. J. Natan, R. G. Freeman, R. P. Van Duyne, and G. C. Schatz. Gold nanoparticle dimer plasmonics: finite element method calculations of the electromagnetic enhancement to surface-enhanced raman spectroscopy. *Analytical and Bioanalytical Chemistry*, 394(7), 2009.

[44] M. D. McMahon, R. Lopez, H. M. Meyer III, L. C. Feldman, and R. F. Haglund Jr. Rapid tarnishing of silver nanoparticles in ambient laboratory air. *Applied Physics B*, 80:915–921, 2005.

[45] G. Mie. articles on the optical characteristics of turbid tubes, especially colloidal metal solutions. *Annalen Der Physik*, 25(3):377–445, 1908.

[46] M. Moskovits. Surface-enhanced spectroscopy. *Reviews in Modern Physics*, 57:783–826, 1985.

[47] M. Moskovits. Surface-enhanced raman spectroscopy: a brief retrospective. *Journal of Raman Spectroscopy*, 36(6-7):485–496, 2005.

[48] M. Moskovits and D. H. Jeong. Engineering nanostructures for giant optical fields. *Chemical Physics Letters*, 397(1-3):91–95, 2004.

[49] K. Nagayama. Two-dimensional self-assembly of colloids in thin liquid films. *Colloids and Surfaces A*, 109:363–374, 1996.

[50] N. L Nguyen, V. V Le, D. K. Chu, C. D. Sai, T. N. Cao, T. H. Pham, D. T. Nguyen, and M. Q. Luu. Synthesis and optical properties of colloidal gold nanoparticles. *Journal of Physics: Conference Series*, 187:2026, 2009.

[51] S. M. Nie and S. R. Emery. Probing single molecules and single nanoparticles by surface-enhanced raman scattering. *Science*, 275(5303):1102–1106, 1997.

[52] K. Nielsch, R. B. Wehrspohn, J. Barthel, J. Kirschner, U. Gosele, S. F. Fischer, and H. Kronmuller. Hexagonally ordered 100 nm period nickel nanowire arrays. *Applied Physics Letters*, 79(9):1360–1362, 2001.

[53] P. Nordlander, C. Oubre, E. Prodan, K. Li, and M. I. Stockman. Plasmon hybridizaton in nanoparticle dimers. *Nano Letters*, 4(5):899–903, 2004. Times Cited: 201.

[54] L. Novotny and B. Hecht. *Principles of Nano-Optics*. Cambridge University Press, Cambridge, 2006.

[55] A. Otto. *Surface-enhanced Raman scattering: 'classical' and 'chemical' origins*. Springer Berlin / Heidelberg, Berlin, 1984.

[56] E. K. Payne, K. L. Shuford, S. Park, G. C. Schatz, and C. A. Mirkin. Multipole plasmon resonances in gold nanorods. *Journal of Physical Chemistry B*, 110(5):2150–2154, 2006.

[57] M. L. Pedano, S. Z. Li, G. C. Schatz, and C. A. Mirkin. Periodic electric field enhancement along gold rods with nanogaps. *Angewandte Chemie-International Edition*, 49(1):78–82, 2010.

[58] D. Pines. Collective energy losses in solids. *Reviews of Modern Physics*, 28:184–199, 1956.

[59] E. Prodan, C. Radloff, N. J. Halas, and P. Nordlander. A hybridization model for the plasmon response of complex nanostructures. *Science*, 302(5644):419–422, 2003.

[60] L. Qin, M. J. Banholzer, J. E. Millstone, and C. A. Mirkin. Nanodisk codes. *Nano Letters*, 7(12):3849–3853, 2007.

[61] L. D. Qin, S. L. Zou, C. Xue, A. Atkinson, G. C. Schatz, and C. A. Mirkin. Designing, fabricating, and imaging raman hot spots. *Proceedings of the National Academy of Sciences of the United States of America*, 103(36):13300–13303, 2006.

[62] M. Quinten. Local fields close to the surface of nanoparticles and aggregates of nanoparticles. *Applied Physics B-Lasers and Optics*, 73(3):245–255, 2001.

[63] C. V. Raman and K. S. Krishnan. A new type of secondary radiation. *Nature*, 121:501–502, 1921.

[64] W. Rechberger, A. Hohenau, A. Leitner, J. R. Krenn, B. Lamprecht, and F. R. Aussenegg. Optical properties of two interacting gold nanoparticles. *Optics Communications*, 220(1-3):137–141, 2003.

[65] J. P. Rolland, E. C. Hagberg, G. M. Denison, K. R. Carter, and J. M. De Simone. High-resolution soft lithography: Enabling materials for nanotechnologies. *Angewandte Chemie-International Edition*, 43(43):5796–5799, 2004.

[66] J. P. Rolland, B. W. Maynor, L. E. Euliss, A. E. Exner, G. M. Denison, and J. M. DeSimone. Direct fabrication and harvesting of monodisperse, shape-specific nanobiomaterials. *Journal of the American Chemical Society*, 127(28):10096–10100, 2005.

[67] M. J. Rust. Nanoparticle assemblies on nanoinjection-molded polymer templates. *IEEE Transactions on Nanotechnology*, 9(1):93–96, 2010.

[68] R. Sardar, T. B. Heap, and J. S. Shumaker-Parry. Versatile solid phase synthesis of gold nanoparticle dimers using an asymmetric functionalization approach. *Journal of the American Chemical Society*, 129(17):5356–+, 2007.

[69] Y. Sawai, B. Takimoto, H. Nabika, K. Ajito, and K. Murakoshi. Observation of a small number of molecules at a metal nanogap arrayed on a solid surface using surface-enhanced raman scattering. *Journal of the American Chemical Society*, 129(6):1658–1662, 2007.

[70] C. Schonenberger, B. M. I. vanderZande, L. G. J. Fokkink, M. Henny, C. Schmid, M. Kruger, A. Bachtold, R. Huber, H. Birk, and U. Staufer. Template synthesis of nanowires in porous polycarbonate membranes: Electrochemistry and morphology. *Journal of Physical Chemistry B*, 101(28):5497–5505, 1997.

[71] H. W. Schrotter and H. W. Klockner. *Raman scattering cross-sections in gases and liquids*. Springer, Berlin, 1979.

[72] K. H. Su, Q. H. Wei, X. Zhang, J. J. Mock, D. R. Smith, and S. Schultz. Interparticle coupling effects on plasmon resonances of nanogold particles. *Nano Letters*, 3(8):1087–1090, 2003.

[73] Z. Q. Tian. General discussion. *Faraday Discuss.*, 132:85–94, 2006.

[74] Z. B. Wang, B. S. Luk'yanchuk, W. Guo, S. P. Edwardson, D. J. Whitehead, L. Li, Z. Liu, and K. G. Watkins. The influences of particle number on hot spots in strongly coupled metal nanoparticles chain. *Journal of Chemical Physics*, 128(9), 2008.

[75] H. Wei, A. Reyes-Coronado, P. Nordlander, J. Aizpurua, and H. Xu. Multipolar plasmon resonances in individual ag nanorice. *ACS Nano*, 4(5):2649–2654, 2010.

[76] C. M. Whelan, M. R. Smyth, and C. J. Barnes. Hreels, xps, and electrochemical study of benzenethiol adsorption on au(111). *Langmuir*, 15(1):116–126, 1999.

[77] G. M. Whitesides, E. Ostuni, S. Takayama, X. Y. Jiang, and D. E. Ingber. Soft lithography in biology and biochemistry. *Annual Review of Biomedical Engineering*, 3:335–373, 2001.

[78] K. L Wustholz, A. I. Henry, J. M. McMahon, R. G. Freeman, N. Valley, M. E. Piotti, M. J. Natan, G. C. Schatz, and R. P. Van Duyne. Structure-activity relationships in gold nanoparticle dimers and trimers for surface-enhanced raman spectroscopy. *Journal of the American Chemical Society*, 132(31):10903–10910, 2010.

[79] Y. N. Xia, J. J. McClelland, R. Gupta, D. Qin, X. M. Zhao, L. L. Sohn, R. J. Celotta, and G. M. Whitesides. Replica molding using polymeric materials: A practical step toward nanomanufacturing. *Advanced Materials*, 9(2):147–149, 1997.

[80] Y. N. Xia and G. M. Whitesides. Soft lithography. *Angewandte Chemie-International Edition*, 37(5):551–575, 1998.

[81] Y. N. Xia, Y. D. Yin, Y. Lu, and J. McLellan. Template-assisted self-assembly of spherical colloids into complex and controllable structures. *Advanced Functional Materials*, 13(12):907–918, 2003.

[82] H. X. Xu. A new method by extending mie theory to calculate local field in outside/inside of aggregates of arbitrary spheres. *Physics Letters A*, 312(5-6):411–419, 2003.

[83] H. X. Xu. A new method by extending mie theory to calculate local field in outside/inside of aggregates of arbitrary spheres. *Physics Letters A*, 312(5-6):411–419, 2003.

[84] H. X. Xu. Calculation of the near field of aggregates of arbitrary spheres. *Journal of the Optical Society of America a-Optics Image Science and Vision*, 21(5):804–809, 2004.

[85] H. X. Xu, J. Aizpurua, M. Kall, and P. Apell. Electromagnetic contributions to single-molecule sensitivity in surface-enhanced raman scattering. *Physical Review E*, 62(3):4318–4324, 2000.

[86] H. X. Xu, E. J. Bjerneld, M. Kall, and L. Borjesson. Spectroscopy of single hemoglobin molecules by surface enhanced raman scattering. *Physical Review Letters*, 83(21):4357–4360, 1999.

[87] H. X. Xu and M. Kall. Surface-plasmon-enhanced optical forces in silver nanoaggregates. *Physical Review Letters*, 89(24), 2002.

[88] Y. Yadong and Y. Xia. Self-assembly of monodispersed spherical colloids into complex aggregates with well-defined sizes, shapes, and structures. *Advanced Materials*, 13(4):267–271, 2001.

[89] H. Yang, P. Deschatelets, S. T. Brittain, and G. M. Whitesides. Fabrication of high performance ceramic microstructures from a polymeric precursor using soft lithography. *Advanced Materials*, 13(1):54–+, 2001.

[90] Wenhua Yu. *Electromagnetic Simulation Techniques Based on the FDTD Method*. Wiley, New York, 2009.